Disentangling Competitive and Synergistic Chemical Reactivities During the Seeded Growth of High Entropy Alloys on High Entropy Metal Sulfide Nanoparticles

Joseph M. Veglak,[1] Aaron Tsai,[1] Samuel S. Soliman,[1] Gaurav R. Dey,[1] and Raymond E. Schaak[1,2,3,*]

[1] *Department of Chemistry,* [2] *Department of Chemical Engineering, and* [3] *Materials Research Institute, The Pennsylvania State University, University Park, PA 16802, United States*

E-mail: res20@psu.edu

ABSTRACT

The seeded growth of one type of nanoparticle on the surface of another is foundational to synthesizing many multi-functional nanostructures. High entropy nanoparticles that randomly incorporate five or more elements offer enhanced properties due to synergistic interactions. Incorporating high entropy nanoparticles into seeded growth platforms is essential for merging their unique properties with the functional enhancements that arise from particle-particle interactions. However, the complex compositions of high entropy materials complicate the seeded growth process due competing particle growth and chemical reactivity pathways. Here, we design and synthesize a 36-member nanoparticle library to identify and disentangle these competitive interactions, ultimately defining chemical characteristics that underpin the seeded growth of high entropy alloys on high entropy metal sulfide nanoparticles. As a model system, we focus on (Cu,Zn,Co,In,Ga)S–SnPdPtRhIr, which combines a high entropy metal sulfide semiconductor with a high entropy alloy catalyst. We study the seeded growth of all possible pairwise combinations of Sn, Pd, Pt, Rh, Ir, and SnPdPtRhIr on the metal sulfides $Cu_{1.8}S$, ZnS, Co_9S_8, $CuInS_2$, $CuGaS_2$, and (Cu,Zn,Co,In,Ga)S, which have comparable morphologies and sizes. Through these studies, we uncover unexpected chemical reactivities, including cation exchange, redox reactions, and diffusion. Reaction temperature, threshold reduction potentials, metal/sulfide chemical reactivity, and the relative strengths of the various bonds that could be formed during particle growth emerge as the primary factors that underpin seeded growth. Finally, we disentangle these competitive and synergistic chemical reactivities to generate a reactivity map that provides practical guidelines for achieving seeded growth in compositionally complex systems.

INTRODUCTION

High entropy alloys, which contain a random mixture of five or more elements in near equimolar ratios, have emerged as next-generation materials for applications in catalysis,[1–4] magnetism,[5,6] energy storage,[7–9] and thermoelectrics[10,11] because of their unique properties that are a direct result of their complex compositions. As one example, nanoparticles of high entropy alloys exhibit a so-called “cocktail” effect of synergistic properties that emerge from collective interactions among the constituent elements, which leads to unique active sites, complex strain profiles, and impaired surface diffusion that can enhance catalytic activity, selectivity, and stability.[1–4] Because of these synergistic properties that are distinct from those of their constituent metals, as well as the anticipated applications that could benefit from these properties, there is significant interest in developing methods to synthesize high entropy alloys, especially as nanoparticles that maximize surface areas and surface-to-volume ratios.

Most mainstream synthetic methods for high-entropy alloys involve high-temperature heating to maximize the impact of configurational entropy and rapid quenching to trap the compositionally complex alloy in its high-temperature disordered state.[12–15] To synthesize nanoparticles, lower-temperature solution-based methods are often preferred, as they can provide better control over particle size and shape while leveraging chemical reactivity to control composition. Solution-based colloidal methods for the synthesis of high entropy alloy nanoparticles are emerging.[16–19] These methods generally involve the simultaneous introduction of a homogeneous metal reagent mixture and translating it to a homogeneous mixture of the metals in the nanoparticles. A typical protocol involves the simultaneous injection of all metal reagents into a heated solvent/stabilizer mixture, which thermally triggers nucleation, reduction, and subsequent growth of high entropy nanoparticles.[20,21] We are quickly learning, though, that the processes by which high entropy nanoparticles form in solution are not as straightforward as the simplicity of the protocol implies. Rather, the differences in chemical reactivities of the various reagents can lead to the initial formation of seeds containing only one or two metals, with others incorporating as the reaction progresses. For example, in the synthesis of colloidal NiPdPtRhIr high entropy alloy nanoparticles, seeds rich in NiPd form first, followed by subsequent incorporation of Pt, Rh, and Ir.[20] This pathway contrasts with that implicated in the synthesis of SnPdPtRhIr under otherwise identical conditions. Here, SnPdPtRhIr nanoparticles instead appear to form through simultaneous reduction and incorporation of all elements.[20]

Several other solution-based pathways can lead to the synthesis of high entropy nanoparticles. For example, simpler two- or three-metal colloidal alloy nanoparticles can seed the growth of alloy shells. After anchoring them to a refractory support, subsequent post-synthetic thermal intermixing transforms these core@shell precursors to high-entropy nanoparticles.[22–24] As another example, colloidal high entropy metal sulfide nanoparticles can be synthesized through a simultaneous multi-cation exchange reaction. Here, a fraction of the soft Cu^+ cations in cation-deficient copper sulfide ($Cu_{1.8}S$) nanoparticles are removed into solution using trioctylphosphine (TOP), a soft base, while harder Zn^{2+}, Co^{2+}, In^{3+}, and Ga^{3+} cations that are all initially present only in solution enter the nanoparticle to maintain charge balance due to the extracted Cu^+. The product of this specific reaction is a high entropy metal sulfide, (Cu,Zn,Co,In,Ga)S, which is a solid solution of $Cu_{1.8}S$, ZnS, CoS, $CuInS_2$, and $CuGaS_2$.[25,26]

The examples in the preceding paragraphs point to our growing realization that the solution-based reactions that lead to the formation of high-entropy nanoparticles are mechanistically diverse and complex. Some pathways involve reactive nanoparticle seeds as intermediates, while others do not. Some colloidal high entropy nanoparticles form through multiple distinct steps, while others appear (over the time scales studied) to form through more direct routes. This diversity of observed reaction pathways is not unexpected, considering that each metal reagent will have a different reaction rate and threshold reaction temperature, as well as a different reduction potential, than each of the other metal reagents. As-yet unknown interactions among the metal reagents, including *in situ* galvanic reactions that dynamically modify the reactive species, could also play a key role in defining the reactions that occur. Much is already known about the chemistry that underpins the solution synthesis of metal nanoparticles, as well as simple two-metal alloy nanoparticles. Increasing the number of metals from two, in a simple alloy, to five, in a high entropy alloy, represents a significant escalation of complexity in chemical reactivity.

As we look ahead to future uses of high entropy alloy nanoparticles, catalysis remains a prominent application, given the documented advantages of synergistic interactions on catalytic performance. When we consider the use of high entropy alloy nanoparticles in catalysis, we must consider how to anchor them onto support materials, as supported nanoparticle catalysts are ubiquitous for maximizing dispersion and stability, as well as for enhancing catalytic performance through particle-support interactions. Pre-made metal and alloy nanoparticles can be deposited onto supports, but it is more common to grow catalytic nanoparticles directly onto supports. For colloidal high entropy alloy nanoparticles synthesized in solution, direct growth on supports (*i.e.*, heterogeneous nucleation and growth) requires translating the complex and diverse mechanistic insights from direct colloidal synthesis (*i.e.*, homogeneous nucleation and growth) to a seeded growth platform. We must therefore consider how the presence of a support material influences the complex reaction chemistry that leads to the formation of high entropy alloy nanoparticles. Put another way, in what ways does the pathway by which a high entropy alloy nanoparticle forms on a support differ from how it forms directly in solution, and what are the key considerations that allow this process to be controlled? There are likely to be multiple competing and/or cooperative chemical processes involved in such reactions. Identifying and disentangling these reactivities is foundational for controlling the outcome of a seeded growth reaction and, more broadly, of a reaction involving so many independent reagents and possible reaction pathways.

Here, we designed and studied a series of model systems to understand how the presence of a support material, *i.e.*, a different nanoparticle seed, influences the formation of a catalytically relevant high entropy alloy nanoparticle. As our primary model system, we chose to study the solution-based seeded growth of a SnPdPtRhIr high entropy alloy on nanoparticles of the high entropy metal sulfide (Cu,Zn,Co,In,Ga)S. We show that (Cu,Zn,Co,In,Ga)S, synthesized by simultaneous multi-cation exchange, is a semiconductor with a visible-wavelength band gap of ~2.2 eV, while SnPdPtRhIr, which can form directly in solution, is an active catalyst for the hydrogen evolution reaction. We began by identifying conditions for growing the high entropy alloy on the high entropy metal sulfide to form (Cu,Zn,Co,In,Ga)S–SnPdPtRhIr, which spatially segregates ten different metals into distinct regions of a nanoparticle. We then deconvoluted this ten-metal system into all possible combinations of its constituent metal sulfides and metals to understand how the compositions of each component influence growth, as well as to identify competitive and synergistic chemical reactivities. The results of these studies, which involve the synthesis, characterization, and analysis of a library of 36 distinct samples, provide important mechanistic insights into seeded growth in compositionally complex systems. These insights lay the groundwork for future advances in the design and synthesis of high entropy nanoparticle catalysts with advanced functions. These studies also reveal unexpected chemical reactivities in compositionally simpler nanoparticle systems and provide chemical insights into how morphology, composition, interfacing, and regioselectivity during seeded growth can be controlled across a diverse set of material systems. The fundamental knowledge gained from this study culminates in a road map that defines and integrates the chemical parameters necessary for controlling compositionally complex seeded growth reactions.

RESULTS AND DISCUSSION

Seeded growth of SnPdPtRhIr on (Cu,Zn,Co,In,Ga)S

We began by designing a modular system where the starting morphology of the seed nanoparticle was the same for all reactions so that we could most reliably elucidate the roles of composition and reaction conditions on facilitating seeded growth. Figure 1 summarizes our approach, which combines cation exchange of $Cu_{1.8}S$ nanoparticles to make a small library of metal sulfide seeds with slow simultaneous injection of reducible metal salt solutions to form metal and alloy nanoparticles. Combining these two approaches allows for independent synthetic control over both the nanoparticle seed and the metal being grown on it. This strategy also allows us to systematically evaluate seeded growth behavior across a library of 36 distinct systems, including (Cu,Zn,Co,In,Ga)S–SnPdPtRhIr, which provides the data necessary to identify and disentangle competitive and synergistic reactivities during high entropy-on-high entropy seeded growth.

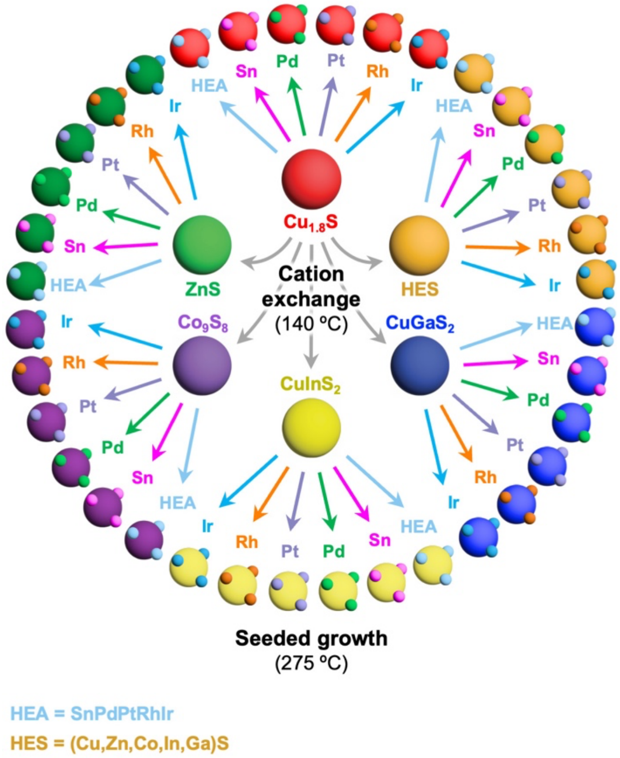

Figure 1. Overview of the high entropy alloy / high entropy metal sulfide nanoparticle library. Schematic depicting the formation of the metal sulfides ZnS, Co_9S_8, $CuInS_2$, and $CuGaS_2$ through cation exchange of $Cu_{1.8}S$ nanoparticles, along with the high-entropy metal sulfide (Cu,Zn,Co,In,Ga)S, which contains $Cu_{1.8}S$, ZnS, Co_9S_8, $CuInS_2$, and $CuGaS_2$ as compositional end members. Six seeded growth reactions can be applied to each of the six types of metal sulfide seeds. These reactions involve the attempted seeded growth of Sn, Pd, Pt, Rh, and Ir, along with the high entropy alloy SnPdPtRhIr. Combining the six reactions with the six types of metal sulfide seeds leads to a library of 36 nanoparticle systems that provide important insights into the competitive and synergistic reactivities involved in high entropy–on–high entropy seeded growth, with 10-metal (Cu,Zn,Co,In,Ga)S–SnPdPtRhIr heterostructured nanoparticles serving as a representative example. In the figure, HES refers to the high entropy sulfide (Cu,Zn,Co,In,Ga)S and HEA refers to the high entropy alloy SnPdPtRhIr.

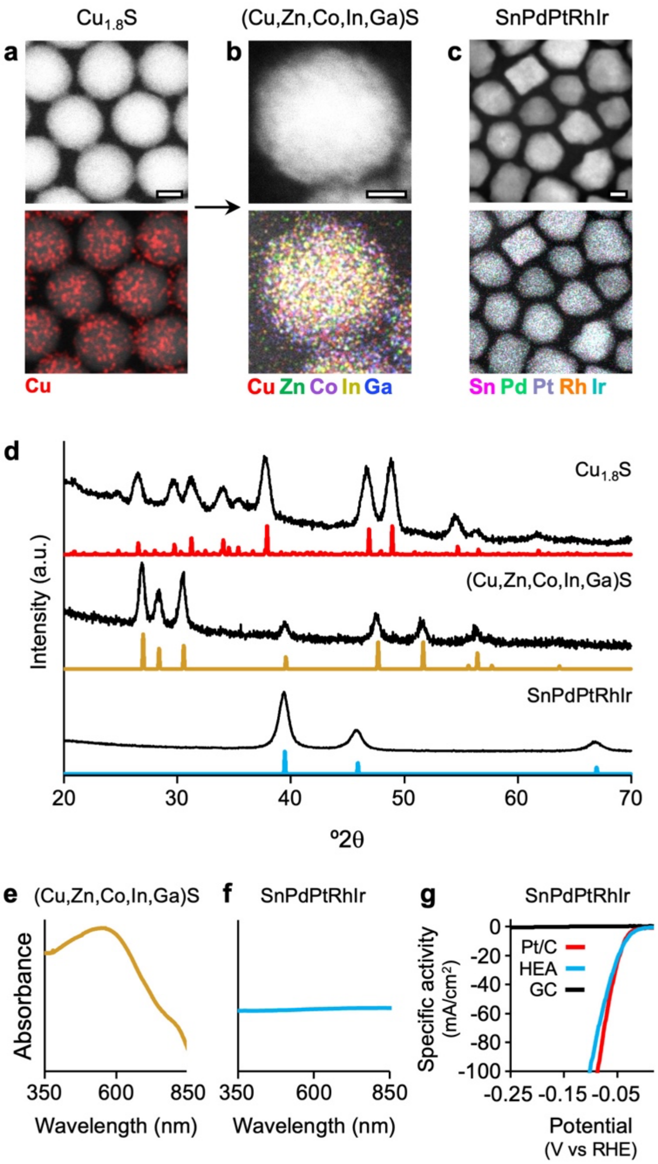

Figure 2. Characterization of stand-alone (Cu,Zn,Co,In,Ga)S and SnPdPtRhIr nanoparticles. HAADF-STEM and STEM-EDS maps of (a) the starting $Cu_{1.8}S$ nanoparticles, (b) the high entropy metal sulfide nanoparticles, (Cu,Zn,Co,In,Ga)S, synthesized through cation exchange of the starting $Cu_{1.8}S$ nanoparticles, and (c) the high entropy alloy nanoparticles, SnPdPtRhIr, made *via* direct synthesis with no metal sulfide seeds present. All scale bars are 5 nm. (d) Experimental (black) and simulated[20,25,27] (colored) XRD patterns for the $Cu_{1.8}S$, (Cu,Zn,Co,In,Ga)S, and SnPdPtRhIr nanoparticles shown in panels (a), (b), and (c). The UV-visible absorption spectrum for (Cu,Zn,Co,In,Ga)S in (e) is consistent with a semiconducting material with a band gap of ~2.2 eV, while the UV-visible absorption spectrum for SnPdPtRhIr in (f) shows a flat optical absorbance across the entire visible range, which is in line with the metallic behavior expected for the high entropy alloy. (g) Linear sweep voltammetry (LSV) data for the SnPdPtRhIr nanoparticles (blue) shows electrocatalytic activity for the hydrogen evolution reaction in acid (0.5 M H_2SO_4) that is on par with that of Pt/C (red). LSV data for a bare graphitic carbon electrode is also shown (black) for comparison.

Figures 2a and 2b show HAADF-STEM images and STEM-EDS element maps of the starting $Cu_{1.8}S$ nanoparticles and the $Cu_{1.8}S$ nanoparticles after simultaneous multi-cation partial exchange with Zn^{2+}, Co^{2+}, In^{3+}, and Ga^{3+} to form the high entropy metal sulfide (Cu,Zn,Co,In,Ga)S.

Particle size and morphology are retained throughout the cation exchange reaction. Figure 2c shows a HAADF-STEM image and STEM-EDS element maps of the high entropy alloy SnPdPtRhIr, which was formed through slow injection (over 10 minutes) at 275 ºC of an oleylamine solution containing $SnCl_2$, $Pd(acac)_2$, $Pt(acac)_2$, $Rh(acac)_3$, and $IrCl_4$, followed by cooling to 200 ºC and quenching with a water bath. Additional characterization data for (Cu,Zn,Co,In,Ga)S and SnPdPtRhIr are shown in Figures S1 and S2 of the Supporting Information. The STEM-EDS data for (Cu,Zn,Co,In,Ga)S and SnPdPtRhIr confirm that for each type of nanoparticle, all five metals are co-localized. Additionally, the corresponding XRD data in Figure 2d confirm single-phase roxbyite $Cu_{1.8}S$, wurtzite (Cu,Zn,Co,In,Ga)S, and face centered cubic (fcc) SnPdPtRhIr. The UV-Visible absorption data in Figure 2e indicate that (Cu,Zn,Co,In,Ga)S is a semiconductor with a visible-wavelength band gap of 2.2 eV while SnPdPtRhIr (Figure 2f) has no detectable band gap, consistent with its expected metallic behavior. Linear sweep voltammetry data (Figure 2g) indicate that SnPdPtRhIr is an active electrocatalyst for the hydrogen evolution reaction in acid. SnPdPtRhIr/C exhibits overpotentials of 34 and 103 mV at current densities of 10 and 100 mA/cm^2, respectively, which are on par with those of a Pt/C control.

We next sought to initiate seeded growth of the high entropy alloy on the high entropy metal sulfide by first introducing the (Cu,Zn,Co,In,Ga)S nanoparticles into the solvent mixture used for the high entropy alloy synthesis, followed by slow injection of the high entropy alloy reagents under the same conditions used to make the SnPdPtRhIr nanoparticles. A powder XRD pattern for the nanoparticles isolated from this reaction, shown in Figure 3a, matches well with a combination of a wurtzite pattern having hexagonal lattice parameters of a = 3.81 Å and c = 6.28 Å and a fcc pattern having a cubic lattice parameter of a = 4.05 Å. The values of the lattice constants are intermediate among the end members and match well with those calculated in previous reports,[20,25] as described in detail in Table S1 of the Supporting Information, and are therefore consistent with the presence of both wurtzite (Cu,Zn,Co,In,Ga)S and fcc SnPdPtRhIr in the sample. We note that in the XRD patterns for high entropy materials, minor peak shifts can sometimes be observed relative to those expected based on the weighted average of the end members; these correlate with the slight sample-to-sample variations in composition that can occur during synthesis.

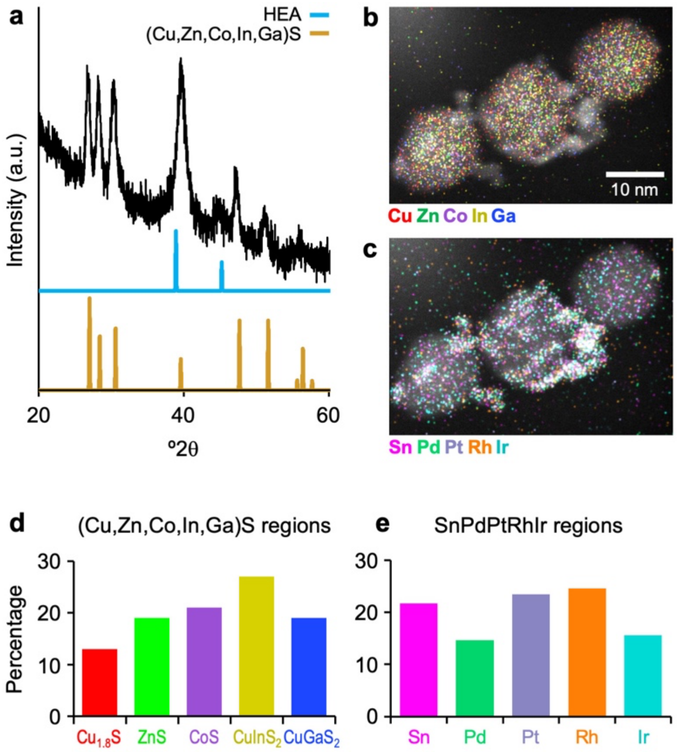

Figure 3. Characterization of (Cu,Zn,Co,In,Ga)S–SnPdPtRhIr high entropy metal sulfide / high entropy alloy nanoparticles. (a) XRD pattern of the synthesized (Cu,Zn,Co,In,Ga)S–SnPdPtRhIr nanoparticles, along with the reference patterns for SnPdPtRhIr[20] and (Cu,Zn,Co,In,Ga)S.[25] STEM-EDS element maps showing the (b) (Cu,Zn,Co,In,Ga)S and (c) SnPdPtRhIr regions of several (Cu,Zn,Co,In,Ga)S–SnPdPtRhIr nanoparticles. These element maps confirm the co-localization of the five elements in the high entropy metal sulfide seed and the five elements in the high entropy alloy regions. The percent compositions of each of the five end members that comprise (Cu,Zn,Co,In,Ga)S are provided in the bar chart in panel (d) while the percent compositions of the SnPdPtRhIr regions are provided in the bar chart in panel (e). The percentages were calculated based on the elemental compositions provided from quantifying the EDS data in panels (b) and (c).

The HAADF-STEM and STEM-EDS data in Figures 3b-c confirm that the high entropy metal sulfide and the high entropy alloy are connected to one another, and therefore that the seeded growth reaction was successful. The (Cu,Zn,Co,In,Ga)S seed particle remains intact, with a co-localized distribution of elements and a composition (by EDS) of $Zn_{0.12}Co_{0.13}In_{0.17}Ga_{0.13}Cu_{0.45}S$. It is important to note that the amount of Cu is higher than the other cations due to the nature of both the In^{3+} and Ga^{3+} cation exchange reactions, where the final products are $CuInS_2$ and $CuGaS_2$, respectively. In both cases, every In^{3+} or Ga^{3+} cation that is exchanged into the nanoparticle requires one Cu^+ cation to remain associated with it to provide charge balance. Additionally, some $Cu_{1.8}S$ remains unexchanged, and this component has close to two copper cations for every one sulfur anion. Given all of these considerations (as described in more detail in the Supporting Information), the composition determined by EDS is consistent with near-equimolar ratios of the end members ZnS (19%), CoS (21%), $CuInS_2$ (27%), $CuGaS_2$ (21%), and $Cu_{1.8}S$ (13%) (Figure 3d). Additional discussion and characterization (Figure S3) is provided in the Supporting Information. The smaller particles observed to be growing on the surface of the (Cu,Zn,Co,In,Ga)S seed particle have co-localized signals from the L lines of Sn, Pd, Pt, Rh, and Ir. The composition, based on analysis of the EDS data, is $Sn_{0.22}Pd_{0.15}Pt_{0.24}Rh_{0.25}Ir_{0.16}$ (Figure 3e), which is consistent with the targeted high entropy alloy. Collectively, the data in Figure 3 are consistent with the successful seeded growth of high entropy alloy nanoparticles on high entropy metal sulfide nanoparticles, which can be described as (Cu,Zn,Co,In,Ga)S–SnPdPtRhIr. It is notable that under the reaction conditions used here, only high entropy alloys grew on the (Cu,Zn,Co,In,Ga)S seeds, rather than the individual constituent metals or simpler metal alloys. However, if higher concentrations of the reagents used to grow SnPdPtRhIr were used, then SnPdPtRhIr would form as large, agglomerated particles. In such a case, we would not be able to differentiate formation through a homogeneous nucleation and growth pathway or through seeded growth, as shown in Figure S4. We therefore keep concentration constant in all subsequent studies.

Temperature and Time Studies

To provide additional information about the reaction conditions required for achieving seeded growth of a high entropy alloy on a high entropy metal sulfide, as well as to begin gaining reaction pathway insights, we carried out the same reaction described above, but at different times and temperatures; the data from these studies are shown in Figures 4 and S5-S9. The seeded growth reactions used to generate the data in Figures 2 and 3 were carried out at 275 ºC for 10 min. At 275 ºC (Figure 4a), a reaction quenched after only 3 min shows small metal particles growing on the sulfide seeds, which is consistent with the early stages of SnPdPtRhIr growth on (Cu,Zn,Co,In,Ga)S. The corresponding STEM-EDS map, along with an accompanying line scan, confirms that the small metal particles do indeed contain co-localized Sn, Pd, Pt, Rh, and Ir, while Cu, Zn, Co, In, and Ga are co-localized in the (Cu,Zn,Co,In,Ga)S region.

At the longer time point of 70 min, SnPdPtRhIr continues to grow on (Cu,Zn,Co,In,Ga)S, as shown in Figures 4b and S6. Not unexpectedly, shorter reaction times provide synthetic access to the smallest high entropy alloy nanoparticles anchored onto the high entropy metal sulfide supports, but it is notable that the high entropy alloy seems to form and grow early in the reaction, as confirmed in Figure 4a. Decreasing the temperature to 180 ºC, a 3-min time point shows evidence of Pt and Pd growing on the surface of the (Cu,Zn,Co,In,Ga)S seeds (Figure S7). At 10 min (Figure 4c) and 40 min (Figure S9), we begin to see the growth of Rh and Ir. Interestingly, while Rh and Ir are always co-localized with one another, they are not always co-localized with Pt or Pd. By 70 min, the (Cu,Zn,Co,In,Ga)S seeds containing small metal particles are accompanied by free-standing metal particles containing a Pt core with a shell containing Rh, Ir, and/or Pd (Figure 4d). Line scans across the freestanding particles in Figure 4d confirm that they consist of Ir and Rh surrounding a Pt core, while Pd is mixed with both the Pt and the Rh and Ir regions. Furthermore, Co and Ga unexpectedly appear within the metal alloy regions, suggesting that throughout the course of the reaction, Co and Ga are pulled out of the metal sulfide seed and incorporated into the metal alloy. It is also noteworthy that the spatial distribution of metals in the (Cu,Zn,Co,In,Ga)S seeds changes, with some elements localized more toward the center and others enriched toward the outer region of the particles. Finally, for all of the attempted seeded growth reactions carried out at 180 ºC, no Sn is observed in any of the metal particles, suggesting that higher temperatures are necessary for Sn^{2+} to reduce to Sn. Consistent with this hypothesis, additional 10-min reactions at intermediate temperatures (225 ºC and 250 ºC) show that Sn does not incorporate at 225 ºC but does starting at 250 ºC (Figures S10 and S11).

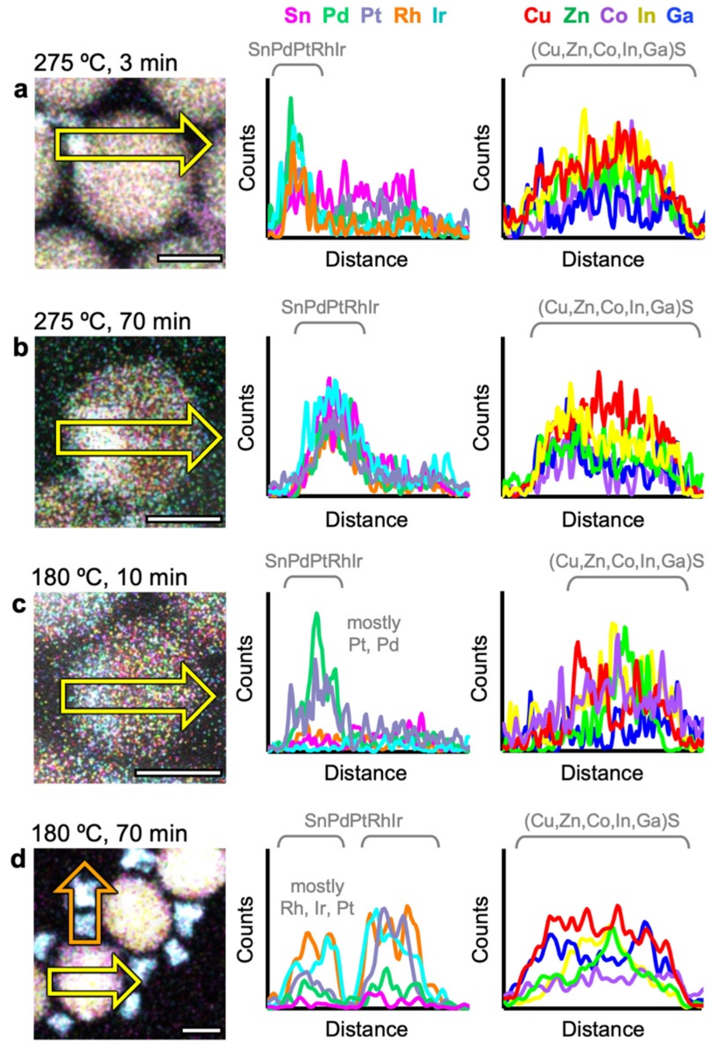

Figure 4. Single-particle characterization at different reaction times and temperatures. High-resolution STEM-EDS element maps and accompanying line scans (as shown by the arrows) of (Cu,Zn,Co,In,Ga)S–SnPdPtRhIr nanoparticles synthesized at different reaction times and temperatures. The line scans for the particles synthesized at 275 ºC for (a) 3 minutes and (b) 70 minutes show colocalization of all elements that comprise both the high entropy alloy and the high entropy metal sulfide. In contrast, the line scans for the particles synthesized at 180 ºC for (c) 10 minutes and (d) 70 minutes reveal phase segregation, incomplete metal incorporation in the high entropy alloy, and/or changes in the composition of the high entropy metal sulfide. All scale bars are 10 nm.

Comparison of the results of attempted SnPdPtRhIr growth on (Cu,Zn,Co,In,Ga)S at different temperatures and times highlights several important considerations for achieving successful seeded growth of high entropy alloys. First, given how many metals are present, it is important to consider threshold reaction and/or reduction temperatures. Incorporating Sn, for example, requires a higher temperature, so all other metals (and their reactivities and rates of reduction) must be compatible with the higher temperature. Second, temperature and time can both influence heterogeneous vs homogeneous nucleation and growth (*i.e.*, seeded growth vs unseeded particle formation), as well as the formation of heterogeneous particles vs. alloy particles with homogeneous co-localization of all elements. In that regard, these temperature and time studies also indicate that it is necessary for all five metals to reduce simultaneously to form the SnPdPtRhIr high entropy alloy and avoid the phase segregation seen at lower temperatures and shorter times. Third, at sufficiently high temperatures, high entropy alloy particles appear to form at early time points, indicating that the smallest particles (that maximize accessible surface area, as is advantageous for applications in catalysis) can be formed with short reaction times, despite their compositional complexity. Fourth, composition and morphology can evolve with time and temperature, suggesting that accelerated optimization studies (such as Design of Experiments[28] or Bayesian Optimization[29]) may be helpful. Finally, the seed can be reactive under certain conditions, given the complex mixture of metal reagents that is present. In the examples in Figure 4, we observe some changes in the morphology of the seed, as well as composition changes via incorporation of some elements from the seed into the growing high entropy alloy particles. These insights motivate our studies in the sections below, which include systematic investigations into the seeded growth of SnPdPtRhIr on the individual constituent metal sulfide nanoparticles ($Cu_{1.8}S$, ZnS, Co_9S_8, $CuInS_2$, and $CuGaS_2$), as well as each individual constituent metal in the high entropy alloy (Sn, Pd, Pt, Rh, and Ir) on the high entropy metal sulfide seed, (Cu,Zn,Co,In,Ga)S, and on each individual constituent metal sulfide.

Seeded growth of SnPdPtRhIr on Constituent Metal Sulfide Nanoparticles

Given the observations noted above, we next sought to understand the growth behaviors of the high entropy alloy, SnPdPtRhIr, on each of the individual constituent metal sulfides that comprise (Cu,Zn,Co,In,Ga)S. Using $Cu_{1.8}S$ nanoparticles having the same sizes and morphologies as those used to make (Cu,Zn,Co,In,Ga)S through simultaneous multi-cation exchange, we carried out cation exchange reactions with the individual metals to make ZnS, Co_9S_8, $CuInS_2$, and $CuGaS_2$. We then subjected each of these five metal sulfide nanoparticle samples ($Cu_{1.8}S$, ZnS, Co_9S_8, $CuInS_2$, and $CuGaS_2$), which all have comparable sizes and morphologies (Figure S12), to the conditions used in Figure 1 to attempt to grow SnPdPtRhIr. It should be noted that the cobalt-containing end member in (Cu,Zn,Co,In,Ga)S, which adopts a wurtzite crystal structure, is wurtzite CoS, which is metastable. Under the temperatures required for seeded growth, CoS converts to Co_9S_8. Therefore, we consider Co_9S_8 as the relevant end member for seeded growth and designate it as the “compositional end member” of (Cu,Zn,Co,In,Ga)S.

Figure 5 shows HAADF-STEM, STEM-EDS maps with corresponding line scans, and XRD data summarizing the results of attempted growth of SnPdPtRhIr on $Cu_{1.8}S$, ZnS, Co_9S_8, $CuInS_2$, and $CuGaS_2$ nanoparticle seeds; additional data are provided in Figures S13-S17 of the Supporting Information. Briefly, for all systems in Figure 5, the HAADF-STEM and STEM-EDS data show evidence of an intact metal sulfide seed along with the successful growth of metal particles, while XRD shows evidence of the metal sulfide seed and an additional fcc phase. Upon analyzing the data in greater depth, several key observations emerge.

First, based on the STEM-EDS element maps and the corresponding line scans, the high entropy alloy SnPdPtRhIr forms in all systems. All five elements incorporate and co-localize, indicating that the fcc phases seen by XRD for all samples correspond to SnPdPtRhIr. This observation confirms that the conditions that enable homogeneous nucleation and growth of the high entropy alloy are also compatible with heterogeneous nucleation and growth.

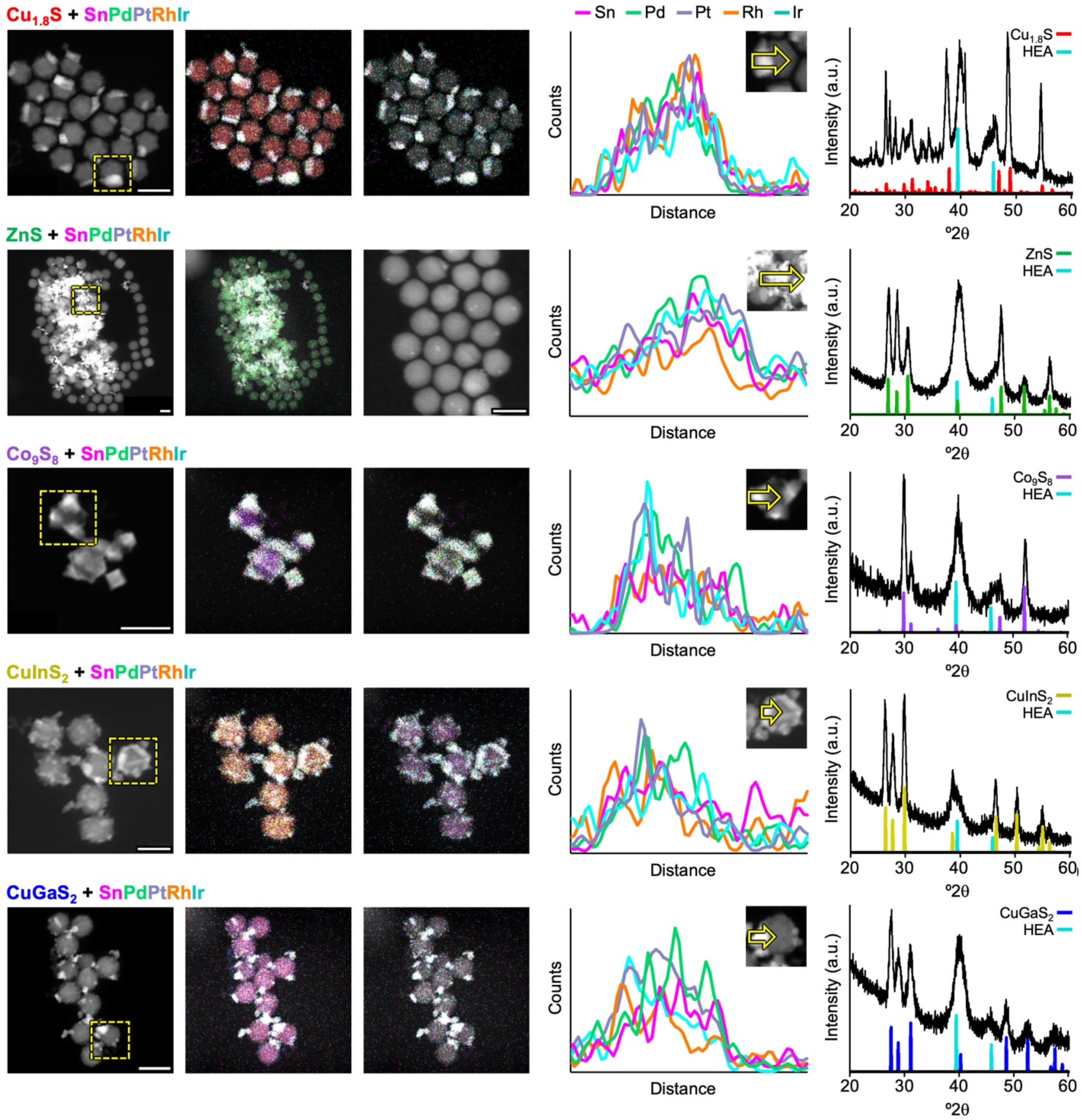

Figure 5. Seeded growth of SnPdPtRhIr on metal sulfide nanoparticles. HAADF-STEM images, STEM-EDS element maps, line scans of individual particles (as indicated by the arrow in the region highlighted by a dashed yellow box), and XRD data are provided for the products obtained after attempted seeded growth of SnPdPtRhIr[20] onto each of the individual metal sulfides ($Cu_{1.8}S$,[27] ZnS,[30] Co_9S_8,[31] $CuInS_2$,[32] and $CuGaS_2$[33]). Two sets of STEM-EDS element maps are provided; the first includes signals from the metals in the metal sulfide as well as in the high entropy alloy, while the second includes only the metals in the high entropy alloy overlaid on the HAADF-STEM image. The STEM-EDS data along with the line scans confirm incorporation and colocalization of all five metals within the high entropy alloy regions. The XRD data confirm both the presence of the metal sulfide and the high entropy alloy throughout the bulk sample. For the ZnS sample, only a single STEM-EDS element map is provided, along with an additional HAADF-STEM image, because the SnPdPtRhIr prefers to agglomerate and grow at fewer sites, leaving most of the ZnS nanoparticles without SnPdPtRhIr. All scale bars are 20 nm.

Second, the morphologies of the ZnS, $CuGaS_2$, and $CuInS_2$ seeds remain largely unchanged after growth of SnPdPtRhIr, but the $Cu_{1.8}S$ and Co_9S_8 seeds appear to become more faceted. To probe this observation further, we carried out a series of control reactions where the $Cu_{1.8}S$ and Co_9S_8 nanoparticle seeds were subjected to the reaction conditions used to grow SnPdPtRhIr, but without any of the metal salts present. HAADF-STEM images from these control experiments, shown in Figure S18, reveal that the Co_9S_8 nanoparticles agglomerate, while the $Cu_{1.8}S$ nanoparticles do not. However, despite the differences in agglomeration behavior (which likely correlate with stability of the ligands on the various nanoparticle surfaces), the morphology change for $Cu_{1.8}S$ does not appear to be due to the reaction conditions, but rather to the presence of the metals. For Co_9S_8, we speculate that the surface ligands may bind weaker to the Co_9S_8 seeds than to the other sulfides, since Co_9S_8 contains both Co^{2+} and Co^0; such behavior would accelerate agglomeration.

Finally, across the different metal sulfide seeds, there are differences in the locations of the SnPdPtRhIr particles, as well as how many SnPdPtRhIr particles are present per metal sulfide seed. The $CuInS_2$–SnPdPtRhIr, $CuGaS_2$–SnPdPtRhIr, and Co_9S_8–SnPdPtRhIr systems appear most similar to the (Cu,Zn,Co,In,Ga)S–SnPdPtRhIr system in Figure 2, in terms of the presence of multiple SnPdPtRhIr particles of different sizes surrounding the metal sulfide seed particle. $Cu_{1.8}S$–SnPdPtRhIr, in contrast, has only one SnPdPtRhIr particle per $Cu_{1.8}S$ seed. When we consider how $Cu_{1.8}S$ differs most significantly from ZnS, Co_9S_8, $CuInS_2$, and $CuGaS_2$, we note that $Cu_{1.8}S$ has a high vacancy concentration that makes it amenable to cation exchange under similar conditions. It is known that Pt^{2+} and Pd^{2+} cations are capable of cation exchange[34] and for Pd^{2+} exchange of $Cu_{1.8}S$, it has been shown that exchange initiates from a single domain.[35] We therefore hypothesize that Pt and Pd may similarly react at the $Cu_{1.8}S$ nanoparticle surface to form a single domain, but subsequently favor incorporation of the other metals rather than proceed with cation exchange; we further address this possibility in subsequent sections.

The growth of SnPdPtRhIr on ZnS differs as well from growth on the other sulfides. Most notable is the presence of large amounts of SnPdPtRhIr particles that are agglomerated, along with other regions where almost no SnPdPtRhIr particles are attached to the ZnS. Both cases are believed to form through seed-mediated nucleation and growth, but there appears to be a competition between nucleation of SnPdPtRhIr on ZnS seeds versus continued growth on existing SnPdPtRhIr particles. Consistent with this hypothesis, a sample isolated at 3 minutes after initiating growth of SnPdPtRhIr on ZnS (instead of the 10-minute reaction time that we typically use) shows a mixture of bare ZnS seeds (without attached metal particles) and agglomerated SnPdPtRhIr particles, of which some are anchored to ZnS seeds (Figure S19). Selective growth of SnPdPtRhIr onto established SnPdPtRhIr regions is therefore preferred over nucleation and growth of SnPdPtRhIr across all ZnS seeds. When we consider the rationale for this markedly different growth behavior of SnPdPtRhIr on ZnS versus on $Cu_{1.8}S$, Co_9S_8, $CuInS_2$, and $CuGaS_2$, we turn to redox capabilities. ZnS is the only sulfide among our seed materials that has a fully redox-inactive cation, which suggests that a redox trigger may be involved in the early stages of metal nucleation and growth. Both Cu^+ (in $Cu_{1.8}S$, $CuInS_2$, and $CuGaS_2$) and Co^0 and Co^{2+} in Co_9S_8 will spontaneously oxidize in the presence of noble metal cations, which would concomitantly reduce to initiate nucleation and facilitate subsequent growth. Without the redox trigger for ZnS, there is a higher barrier to nucleation on ZnS compared to the other metal sulfides. Accordingly, the nucleation density of SnPdPtRhIr on ZnS is low and growth of SnPdPtRhIr on existing regions of SnPdPtRhIr is favored.

To summarize this section, we learned that $Cu_{1.8}S$, $CuInS_2$, $CuGaS_2$, and Co_9S_8 will seed the growth of the SnPdPtRhIr. In contrast, ZnS disfavored the seeded growth of SnPdPtRhIr, which instead led to the formation of larger agglomerates of SnPdPtRhIr that were not anchored to ZnS.

Additionally, the $Cu_{1.8}S$ and Co_9S_8 seeds exhibited a morphology change during SnPdPtRhIr growth. In Co_9S_8, the morphology change manifested as agglomeration, which was attributed to surface destabilization at elevated temperatures, while in $Cu_{1.8}S$, hexagonal faceting emerged upon heating in the presence of the metal salts. Despite these observations and rationale, some aspects of the observed seeded growth behavior remain unexplained after analysis of the experiments in this section, including the underlying driving forces for the observed growth patterns (*i.e.*, speckling vs single domains). These will be addressed in subsequent sections.

Seeded Growth of Each Individual Metal on Each Metal Sulfide

The results in the preceding section showed different behaviors for the seeded growth of SnPdPtRhIr on the compositional metal sulfide end members that comprise the high entropy (Cu,Zn,Co,In,Ga)S nanoparticles. Building on these observations, we next sought to study the seeded growth of each individual metal (Sn, Pd, Pt, Rh, Ir) on each individual metal sulfide ($Cu_{1.8}S$, ZnS, Co_9S_8, $CuInS_2$, $CuGaS_2$) under identical conditions. Our goal for these studies was to deconvolute the contributions of each metal to the growth behavior, in both the metal sulfide seed and in the high entropy alloy, as well as to identify any synergistic and competitive reactivities that were implicated in the seeded growth process. To do so, we kept the same reaction conditions used for the seeded growth of SnPdPtRhIr but used only one metal at a time. The results are shown in Figure 6, with additional larger-area TEM images provided in Figure S20. In these figures, we show only TEM images without STEM-EDS element maps, since only one metal was used for each reaction. Here, the differences in contrast in the TEM images are sufficient to determine the locations of the metal sulfide and the metal. Since these are bright field TEM images rather than dark-field HAADF-STEM images, the darker contrast regions in Figure 6 correspond to the more electron dense regions, which are the metals, while the lighter contrast regions correspond to the metal sulfide.

Close inspection of the data in Figure 6 reveals several key observations and trends. One observation that immediately stands out is that there is no evidence for metallic Sn nanoparticles growing on the surfaces of any of the metal sulfide nanoparticles, and the corresponding XRD data also shows no evidence of Sn. However, the TEM images indicate the presence of a shell surrounding all of the metal sulfide particles for which attempted growth of Sn was carried out. This shell is consistent with amorphous tin oxide, which is commonly observed in colloidally synthesized nanoparticles of Sn and Sn-based alloys and intermetallic compounds.[36–38] In such systems, the tin oxide shell, which has been confirmed experimentally by X-ray photoelectron spectroscopy, can form *in situ* due to a spontaneous galvanic reaction between Sn^{2+}, which oxidizes to Sn^{4+}, and a more noble metal cation, which reduces to M^0 as it incorporates into the particle.[37,38] Given the lack of evidence for tin nanoparticles, though, we conclude that metallic Sn can only incorporate into nanoparticles under these reaction conditions when it is present along with other elements, including those within the high entropy alloy. In addition, we had observed in Figure 3 that during attempted seeded growth of SnPdPtRhIr at lower temperature (*i.e.*, 180 ºC instead of 275 ºC), Sn did not incorporate and that the remaining elements (Pd, Pt, Rh, Ir) did not homogeneously mix. Taken together, these results suggest a synergistic relationship between Sn and the other elements in the high entropy alloy: Sn is a key contributor to the formation of the high entropy alloy, but Sn cannot form independently, which is consistent with behavior observed during the direct synthesis of SnPdPtRhIr.[20]

A related observation is that metal-containing particles on the metal sulfide seeds are evident for Pd, Pt, Rh, and Ir. We rationalize the ability to grow Pd, Pt, Rh, and Ir, but not Sn, based on reduction potentials. Pd, Pt, Rh, and Ir are noble metals with cations that are easily reducible to zero valent metals, while Sn^{2+} has a much lower reduction potential that renders it incapable of reducing to Sn^0 under these conditions. However, the growth behavior of Pd, Pt, Rh, and Ir differ from one another. We focus initially on analyzing the systems that form (based on XRD) only metallic fcc Pd, Pt, Rh, and Ir on the metal sulfide seeds, followed by those that react to grow alloys and/or sulfides on the metal sulfide seeds.

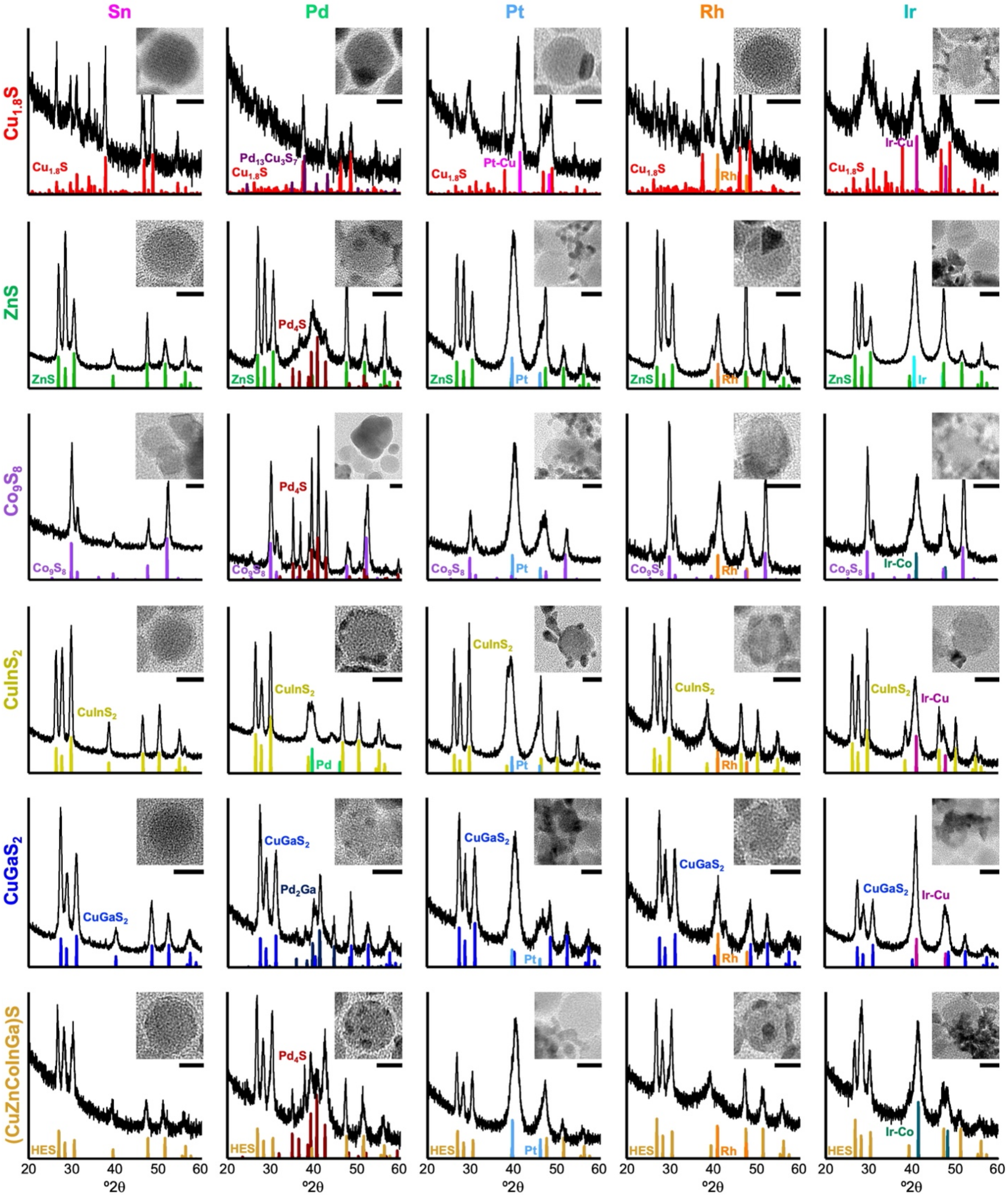

Figure 6. Seeded growth of individual metals on metal sulfide nanoparticles. XRD patterns are shown for all 30 samples generated through attempted seeded growth of Sn, Pd, Pt, Rh, or Ir onto $Cu_{1.8}S$, ZnS, Co_9S_8,

$CuInS_2$, $CuGaS_2$, and (Cu,Zn,Co,In,Ga)S nanoparticles. Reference XRD patterns are also shown and labelled.[20,25,27,30–33,35,39–44] Additional crystal structure information for each reference pattern is compiled in Table S1. Cropped TEM images of individual particles are included in the inset of each XRD pattern to show evidence of the primary type of seeded growth that is observed, ranging from single-particle to multi-particle to agglomerated. Uncropped TEM images are shown in Figure S20. All scale bars are 10 nm.

The XRD data included in Figure 6 show that Pd grows on $CuInS_2$; Pt and Rh grow on ZnS, Co_9S_8, $CuInS_2$, and $CuGaS_2$; and Ir grows on ZnS. We can subdivide these systems into two categories. One category includes metal sulfide seeds that appear to consistently have metal particles on their surfaces. The other category includes mixtures of both bare metal sulfide seeds with no metal particles and large agglomerates of metal particles anchored to a small number of seeds, similar to the behavior observed during the growth of SnPdPtRhIr on ZnS in Figure 5. Closer inspection of these systems reveals that Pt and Ir consistently form large agglomerates of particles while Pd and Rh tend to nucleate and grow on all metal sulfide seeds as discrete particles. Such behavior is a manifestation of the competition between metals preferentially growing on pre-existing metal particles versus nucleating new deposition sites on the metal sulfide seeds. While many factors can be involved in such complex metal growth processes, we look to trends in relevant bond strengths as a proxy for trends in preferential growth behavior, as such correlations have been established previously.[45]

To rationalize these growth behaviors, we consider *M–M* bond strengths. Using gas-phase diatomic bond energies as an estimate, Ir–Ir forms the strongest bond at 361 kJ/mol while the Pt–Pt bond is also comparably strong at 307 kJ/mol. The Rh–Rh bond strength is significantly weaker, at only 235 kJ/mol, and Pd–Pd is even weaker, at around 136 kJ/mol.[46] While numerical values are different for different ways of determining bond energies (*i.e.*, elemental metals, organometallic complexes, etc.), the trends are similar. We can therefore expect that the Ir–Ir and Pt–Pt bonds are generally much stronger than the Rh–Rh and Pd–Pd bonds. The much greater bond energies for Ir–Ir and Pt–Pt relative to Rh–Rh and Pd–Pd correlate with the preference for Ir and Pt to grow off of, and therefore to bond to, itself. Rh and Pd, in contrast, have less of an energetic driving force to behave similarly, instead preferring to anchor to the sulfide surface. Reduction potentials therefore allow us to rationalize which elements grow on the nanoparticle seed and bond strengths help us to rationalize the different growth characteristics of the different metals on the metal sulfide seeds.

For the next stage of our analysis, we consider the differences among the systems that form metals (Pd, Pt, Rh, Ir) during seeded growth versus those that instead form metal sulfides, alloys, or intermetallics, for which chemical reactivity must be implicated. Most notable in Figure 6 is chemical reactivity involving palladium; only $CuInS_2$ grows Pd metal, while $Pd_{13}Cu_3S_7$ forms on $Cu_{1.8}S$, Pd_2Ga forms on $CuGaS_2$ and Pd_4S forms on ZnS and Co_9S_8. Taking into account that Pd–Pd had the weakest M–M bond strength of all four metals, these results are not unexpected, as Pd-based compounds could plausibly form rather than Pd metal. We begin with the $Pd_{13}Cu_3S_7/Cu_{1.8}S$ system. Of all the metal sulfides, $Cu_{1.8}S$ is highly amenable to cation exchange, and $Pd_{13}Cu_3S_7$ has previously been shown to form upon partial Pd^{2+} exchange of $Cu_{1.8}S$ in the presence of an amine using a reaction setup that is similar to ours.[35] We therefore attribute $Pd_{13}Cu_3S_7$ formation on $Cu_{1.8}S$ to partial cation exchange. We rationalize the formation of Pd_4S on ZnS and Co_9S_8 in a similar way. We speculate that under analogous conditions to which Cu^+ was extracted from $Cu_{1.8}S$ and replaced by Pd^{2+} to form $Pd_{13}Cu_3S_7$, oleylamine, a Lewis base, can similarly help to extract small amounts of the stronger Lewis acids Zn^{2+} and Co^{2+}. Palladium then replaces the extracted Zn^{2+} and Co^{2+} to ultimately form Pd_4S, which is the most palladium-rich stable sulfide in the Pd-S phase diagram. Unlike the situation for Pd^{2+} exchange of $Cu_{1.8}S$ forming ternary $Pd_{13}Cu_3S_7$, ternary Pd-Zn-S and Pd-Co-S nanoparticles are not known, so their formation upon Pd^{2+} exchange of ZnS and Co_9S_8, respectively, would be unlikely. We note that the reaction temperature, 275 ºC, is much higher than that of typical cation exchange reactions, which usually occur below 160 ºC. Under the higher-temperature conditions used here, such reactivity, where a 2+ cation can be replaced by another 2+ cation in small amounts, is therefore not unexpected.

For $CuGaS_2$, we propose that some Ga^{3+} is extracted by oleylamine because of the strong Lewis acidity of Ga^{3+} coupled with the high reaction temperature, as discussed above. This process forms Pd_2Ga instead of Pd_4S because Pd_2Ga is a synthetically accessible intermetallic phase at these temperatures (based on the Pd-Ga phase diagram). Comparable Pd-based intermetallics in the other systems (Pd-Co, Pd-Zn) would require higher temperatures and/or harsher reaction conditions (including strong reducing agents) to form. The growth of metallic Pd on $CuInS_2$, which at first glance would be expected to be similar to $CuGaS_2$, is rationalized by considering the lower chemical reactivity of $CuInS_2$ versus $CuGaS_2$. Both In^{3+} and Ga^{3+}, as trivalent cations, have low mobilities and are not typically amenable to cation exchange, but the much stronger Lewis acidity of Ga^{3+} relative to that of In^{3+} allows it to react, while $CuInS_2$ remains intact. The formation of sulfides and intermetallic compounds, rather than metals, on the metal sulfide seeds is therefore rationalized, overall, by cation exchange behavior that is unusual but not unexpected given the high reaction temperature and chemical components of the reaction, combined with competition between the most favorable byproduct phases that will form.

We now turn to systems in Figure 6 where metal alloys form instead of metals; these systems include a Pt-Cu alloy on $Cu_{1.8}S$, Ir-Co alloys on Co_9S_8 and (Cu,Zn,Co,In,Ga)S, and Ir-Cu alloys on $Cu_{1.8}S$, $CuInS_2$ and $CuGaS_2$. Evidence for Pt-Cu, Ir-Co, and Ir-Cu alloy formation comes from the corresponding XRD patterns, where we observe peak shifts to higher 2θ values relative to Pt and Ir, which are indicative of the incorporation of the smaller Cu and Co elements into the larger Pt and Ir unit cells (Figure S21). Additional evidence for alloy formation comes from STEM-EDS maps, which show co-localization of the alloyed elements in the metal particles (Figures S22-S24). We rationalize the formation of Pt-Cu on $Cu_{1.8}S$ as starting with cation exchange. However, given the high temperature and reducing environment that are comparable to conditions used frequently to synthesize PtCu nanocrystals, combined with the lack of prior reports of ternary Pt-Cu-S phases forming upon partial Pt^{2+} exchange of $Cu_{1.8}S$, PtCu forms. When we look at the formation of Ir-Co on Co_9S_8 and Ir-Cu on $Cu_{1.8}S$, $CuInS_2$ and $CuGaS_2$, we note that Ir-Co and Ir-Cu are immiscible alloys in bulk systems. However, there have been reports of alloyed Ir-Cu and Ir-Co nanoparticles that form upon direct co-reduction of solubilized metal salts.[47–49] We already implicated cation exchange (given Lewis acid/base interactions and high temperatures) to drive the initial infiltration of the noble metal cations and the concomitant extraction of Co^{2+} or Cu^{+}. However, unlike for the other systems, the iridium salt contains Ir^{4+}. This Ir^{4+} cation can reduce to an intermediate oxidation state, Ir^{3+}, that could plausibly couple with the oxidation of Cu^{+} to Cu^{2+} in $Cu_{1.8}S$, $CuInS_2$ and $CuGaS_2$ to extract some copper from the metal sulfide seeds or with oxidation of Co^{0} to Co^{2+} in Co_9S_8 and (Cu,Zn,Co,In,Ga)S to extract some cobalt. Given the high temperature and reducing conditions, it is reasonable that solubilized Ir^{3+}/Cu^{2+} and Ir^{3+}/Co^{2+} could then co-reduce to form alloy nanoparticles directly, in accordance with how these bulk-immiscible nanoparticle systems have been reported to form previously.[47–49]

Finally, looking at the Rh growth reactions, the TEM images in Figure 6 show speckled growth on most of the metal sulfides, which is consistent with the XRD data. However, we note that the XRD pattern for Rh growing on $CuInS_2$ shows only $CuInS_2$ and no Rh. Despite this observation, the TEM data shows speckled darker contrast regions consistent with Rh growth. To address this inconsistency, HRTEM data (provided in Figure S25) indicates that the Rh particles are polycrystalline, with small crystalline domains that would result in significant peak broadening in the corresponding XRD pattern. The peaks would be sufficiently broad that they would be largely undetectable in the presence of larger particles of crystalline $CuInS_2$. Through this further analysis, we are confident that $CuInS_2$-Rh does indeed form, even though Rh is not detected by XRD.

Reactivity Map

In the preceding paragraphs, we have rationalized behaviors and trends in attempted individual metal growth reactions on each metal sulfide seed. From this analysis, it is clear that there are competing processes and reactivities. In some cases, metal growth wins out over cation exchange or alloy formation. In other cases, initial cation exchange provides a trigger for nucleation and/or reactivity, and given considerations of chemical reactivities and product stabilities, different products can form. When we combine all of the observations in the preceding figures with the plausible rationale for each that we have provided in the accompanying discussion, the maps in Figure 7 emerge. In Figure 7, we summarize the reactivity trends extracted from the analysis of the data in Figures 5 and 6. Figure 7 provides a graphical summary of the behaviors and trends involving all 36 samples that were analyzed. This figure highlights the interplay between low and high temperature, as well as the growth and reactivity behaviors of individual metals and the high entropy alloy on the various metal sulfide seeds. As such, it provides a visual complement to the data and discussion in all preceding sections and figures.

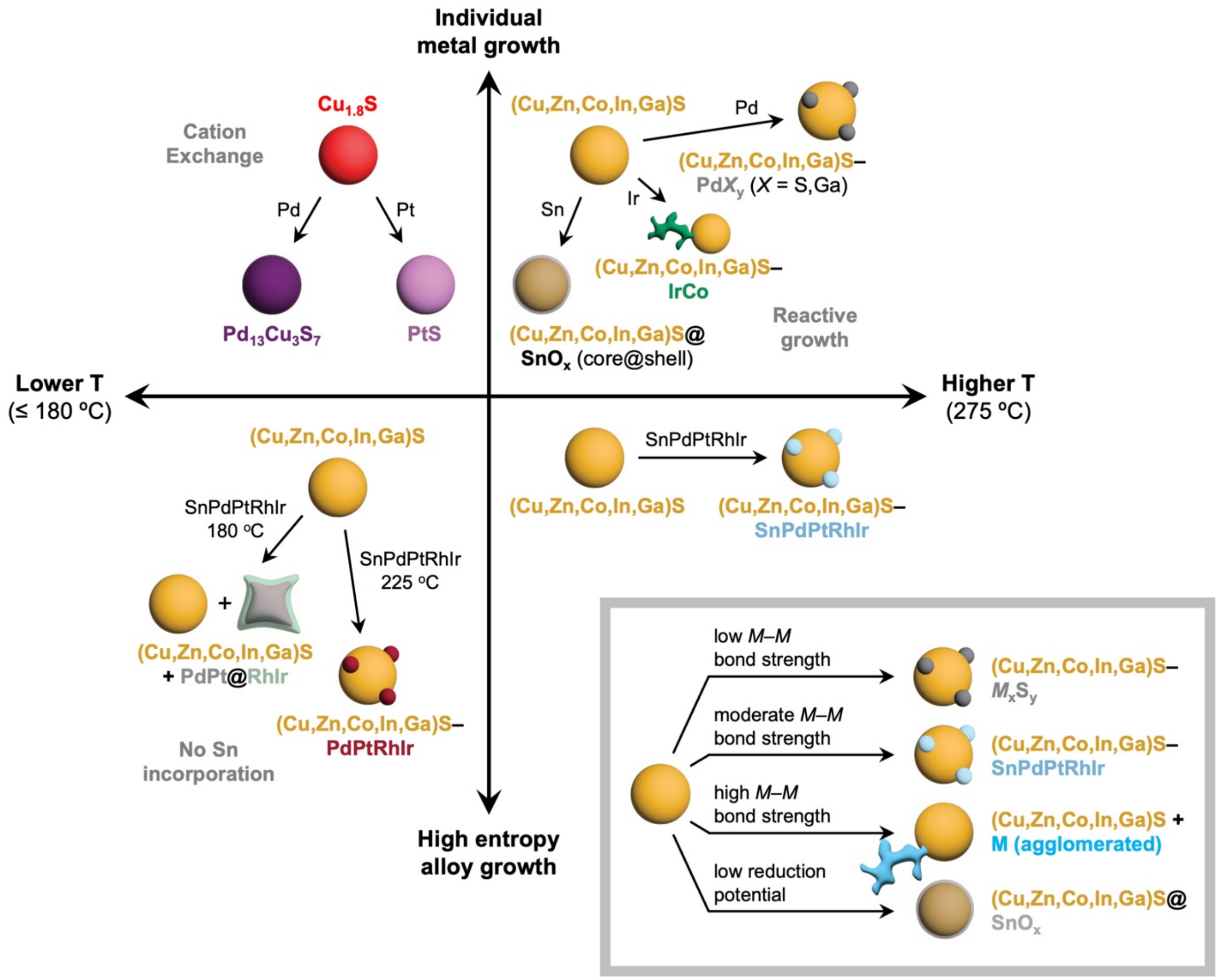

Figure 7. Reactivity map summarizing the key insights into the seeded growth of high entropy alloys on metal sulfide nanoparticles. These insights were gained through studies of how time, temperature, and the metal being reduced influence growth, reactivity, and various product characteristics. The inset in the bottom right summarizes the primary trends (metal-metal bond strengths and reduction potentials, as detailed in the main text) that appear to influence the type of growth, and therefore the composition and morphologies of the products.

To better understand the growth behavior of the (Cu,Zn,Co,In,Ga)S–SnPdPtRhIr reaction, we begin by categorizing each metal individually. Sn incorporates the same on (Cu,Zn,Co,In,Ga)S as it did on each individual metal sulfide seed – as an amorphous tin oxide shell since the reaction conditions are insufficient to reduce Sn^{2+} to Sn^0. Pd forms on (Cu,Zn,Co,In,Ga)S as Pd_4S in much the same way as it did on ZnS and Co_9S_8. This observation suggests that cation exchange can trigger initial incorporation of Pd^{2+} but the presence of the mixture of elements prevents significant penetration of Pd^{2+} into (Cu,Zn,Co,In,Ga)S, as it did in $Cu_{1.8}S$. Additionally, there was no observed rearrangement of the spatial distribution of elements in (Cu,Zn,Co,In,Ga)S, which would be required to generate sufficiently large regions of $Cu_{1.8}S$ to form a product such as $Pd_{13}Cu_3S_7$. The growth of Pt on (Cu,Zn,Co,In,Ga)S appears similar to the growth of Pt on ZnS, Co_9S_8, $CuInS_2$, and $CuGaS_2$, where deposition of Pt on existing Pt seeds outcompetes the nucleation of new Pt domains on the sulfide seeds. The reactivity of Pt on $Cu_{1.8}S$ to form PtCu is not observed on (Cu,Zn,Co,In,Ga)S, indicating that the mixture of Cu^+ with Zn^{2+}, Co^{2+}, In^{3+}, and Ga^{3+} in the high entropy sulfide prevents Cu from migrating and combining with Pt across a large area. Rhodium grows on (Cu,Zn,Co,In,Ga)S in a way that appears analogous to its growth behavior on ZnS, $CuInS_2$ and $CuGaS_2$. This observation suggests that the randomized Cu^+ sites in (Cu,Zn,Co,In,Ga)S, which are mixed with other cations that are unlikely to oxidize, may help to trigger nucleation by locally oxidizing Cu^+ to Cu^{2+} to initiate the reduction of Rh^{3+} to Rh^0. Finally, the growth of iridium on (Cu,Zn,Co,In,Ga)S is most similar to its deposition on Co_9S_8, where the iridium reacts with redox-active cations to form an Ir-Co alloy as confirmed via both XRD (Figure 6) and STEM-EDS (Figure S22).

These comparisons of the growth behaviors of the individual metals on (Cu,Zn,Co,In,Ga)S versus on the constituent metal sulfides provide important insights into the ways in which seeded growth on compositionally complex substrates can be rationalized and predicted based on the behaviors of their constituent components. Most notable from the above discussion are the similarities and differences between deposition behaviors on (Cu,Zn,Co,In,Ga)S versus on $Cu_{1.8}S$. Cu^+ appears to have analogous reactivity in (Cu,Zn,Co,In,Ga)S as it does in $Cu_{1.8}S$ in terms of nucleation, likely serving as a cation exchange or redox trigger for nucleation of other metals and/or compounds. However, in (Cu,Zn,Co,In,Ga)S, Cu^+ is mixed with other cations. Based on the observed reactivity, these other cations appear to pin the Cu^+ in place to prevent it from migrating and forming the larger regions of $Cu_{1.8}S$ that would be necessary to fully mimic on (Cu,Zn,Co,In,Ga)S the growth and reactivity behavior observed on $Cu_{1.8}S$, such as alloy formation or formation of the ternary $Pd_{13}Cu_3S_7$ phase. This characteristic represents a unique synergistic seeded growth behavior for the high entropy sulfide that is not exhibited by the end members.

Now that we have categorized the seeded growth behaviors of each individual constituent metal of SnPdPtRhIr on both (Cu,Zn,Co,In,Ga)S and the metal sulfide end members that comprise it, we can return to the seeded growth of the high entropy alloy SnPdPtRhIr on the high entropy metal sulfide (Cu,Zn,Co,In,Ga)S. As was shown in Figure 3, SnPdPtRhIr grows onto (Cu,Zn,Co,In,Ga)S as multiple small domains rather than as a single large domain, which tracks with the behavior of its growth on Co_9S_8, $CuInS_2$, and $CuGaS_2$, but not on $Cu_{1.8}S$ or ZnS. Our observations for SnPdPtRhIr growth on $Cu_{1.8}S$ seeds pointed to the likelihood that formation of a single large domain is initiated through a small amount of cation exchange that is analogous to the behavior observed in the $Cu_{1.8}S$–Pd and $Cu_{1.8}S$–Pt systems. Therefore, we propose that for the (Cu,Zn,Co,In,Ga)S–SnPdPtRhIr system, similar initial cation exchange behavior of (Cu,Zn,Co,In,Ga)S is unlikely to drive the formation of SnPdPtRhIr. The speckled growth behavior of SnPdPtRhIr is also observed in the Co_9S_8–SnPdPtRhIr, $CuInS_2$–SnPdPtRhIr, and $CuGaS_2$–SnPdPtRhIr systems. The most notable similarity among these metal sulfides is that they contain elements capable of oxidizing: Co^0 in Co_9S_8 and Cu^+ in $CuInS_2$ and $CuGaS_2$.

Given these insights, we attribute the speckled growth behavior of SnPdPtRhIr on (Cu,Zn,Co,In,Ga)S to the presence of multiple oxidation states within the high entropy metal sulfide – some redox active (Cu^+, Co^{2+}) and some redox inactive (Zn^{2+}, In^{3+}, Ga^{3+}) under the deposition conditions. Their random distribution localizes them to certain sites scattered across the surface, with the 3+ cations helping to fix them in place by providing a high barrier to migration. The random mixing of these five different cations would result in discrete redox-active surface sites capable of triggering the reduction, nucleation, and growth of the high entropy alloy throughout these multiple sites across the surface.

Finally, in the bottom right quadrant of Figure 7, we highlight the key trends that lead to the various outcomes when attempting metal growth on (Cu,Zn,Co,In,Ga)S, the high entropy sulfide seed. Considering the relevant bond strengths, we would expect the strongest *M–M* bonds (and/or *M–M'* bonds for different metals) to favor metal growth on existing particles rather than nucleation of new sites, leading to only a small number of particles with large metal domains. Weaker *M–M* or *M–M'* bonds would lead to side products if other *M–X* (*X* = S or Ga) bonds preferentially form. Together, these considerations lead us to conclude that for the high entropy-on-high entropy (Cu,Zn,Co,In,Ga)S–SnPdPtRhIr system, the *M–M* and *M–M'* bonds within the SnPdPtRhIr high entropy alloy must be such that they fall within a range of moderate bond strengths that are intermediate between corresponding *M–M* or *M–M'* bonds and *M–X* bonds, favoring growth onto all (Cu,Zn,Co,In,Ga)S nanoparticles. As one literature example to help validate this hypothesis, it was found in Pt-Sn clusters that Pt-Sn bonds are stronger than Pt-Pt bonds, and as discussed above, Pt-Pt bonds are stronger than Sn-Sn bonds.[50] Applying this data to our system would suggest that Sn incorporates into the high entropy alloy (under conditions where it does not form metallic Sn particles on its own) because growing Sn on Pt is favorable, based on bond strength considerations. Therefore, by applying our understanding of how the individual metals and SnPdPtRhIr grow on the individual metal sulfides, we can deconvolute and rationalize the complex reaction chemistry involved in the growth of SnPdPtRhIr on (Cu,Zn,Co,In,Ga)S to form (Cu,Zn,Co,In,Ga)S–SnPdPtRhIr.

Applicability to regioselective seeded growth of a high entropy alloy

To apply the knowledge gained from all three components of this work – SnPdPtRhIr growth on (Cu,Zn,Co,In,Ga)S, SnPdPtRhIr growth on the compositional metal sulfide end members, and individual metal growth on (Cu,Zn,Co,In,Ga)S and the compositional metal sulfide end members – we now target regioselective growth. Here, we seek to grow SnPdPtRhIr selectively on one metal sulfide when two are present. Partial cation exchange can be leveraged to regioselectively direct seeded growth.[51,52] However, given the compositional complexity of SnPdPtRhIr, its application here is, in principle, a challenging undertaking, since it is plausible that all five individual metals could have different seeded growth preferences and therefore disfavor nucleation and growth of the high entropy alloy. We hypothesized that if we chose one metal sulfide that seeds the growth of a single domain of SnPdPtRhIr and another where growth of SnPdPtRhIr on pre-existing seeds outcompetes the nucleation and growth of new seeds, we could favor seeded growth of SnPdPtRhIr on one metal sulfide and disfavor it on the other. To meet these criteria, we chose $Cu_{1.8}S$, which was shown in Figure 4 to seed the growth of

SnPdPtRhIr, and ZnS, which formed large aggregates of SnPdPtRhIr that were largely disconnected from the metal sulfide. In this system, $Cu_{1.8}S$ (via an initial partial cation exchange trigger) should rapidly seed the growth of SnPdPtRhIr, with continued growth favoring these pre-existing SnPdPtRhIr domains on $Cu_{1.8}S$ rather than generating new domains on ZnS.

To test this hypothesis, we synthesized $Cu_{1.8}S$ nanorods and carried out a partial Zn^{2+} exchange to form $Cu_{1.8}S$–ZnS nanorods. STEM-EDS element maps for the $Cu_{1.8}S$–ZnS nanorods are shown in Figure 8, with additional characterization data shown in Figures S26-S28. We then applied the seeded growth reaction (from Figure 4) used to deposit SnPdPtRhIr on the individual metal sulfides. Figure 8 shows a STEM-EDS map of the product of this reaction. As predicted, SnPdPtRhIr grows exclusively on the $Cu_{1.8}S$ regions of the $Cu_{1.8}S$–ZnS nanorods, with no evidence of growth on the ZnS regions. In addition to providing a rational synthetic pathway to a complex heterostructured nanorod target, this result further validates the utility of the knowledge gained from the studies in the preceding section. We had hypothesized that the aggregates of SnPdPtRhIr that formed on ZnS did so because SnPdPtRhIr prefers to grow on itself rather than on ZnS. On the $Cu_{1.8}S$–ZnS nanorods, this is the exact behavior that was observed, but because SnPdPtRhIr was present on the $Cu_{1.8}S$ regions of almost all of the $Cu_{1.8}S$–ZnS nanorods, SnPdPtRhIr growth was localized to these regions and did not form large aggregates.

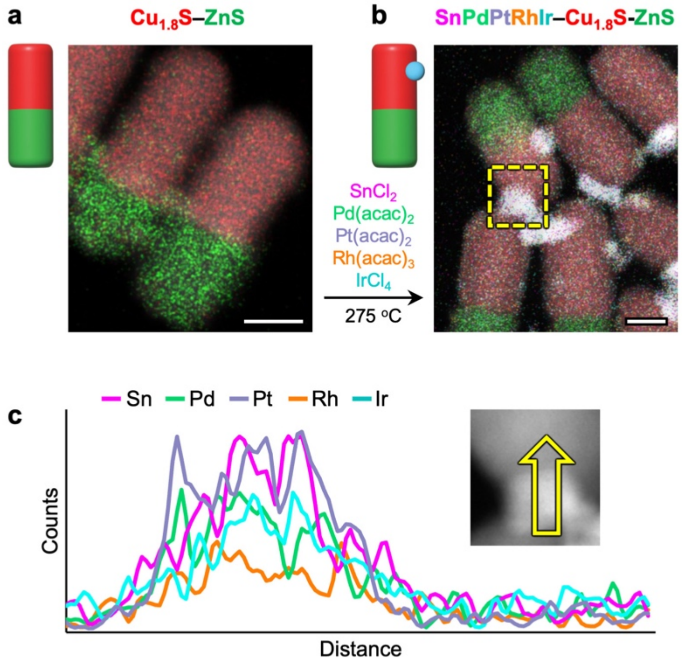

Figure 8. Applicability to regioselective seeded growth. The STEM-EDS element maps show both (a) a starting heterostructured $Cu_{1.8}S$–ZnS nanorod that was used as a seed and (b) the same sample of $Cu_{1.8}S$–ZnS nanorods after being subjected to the SnPdPtRhIr growth reaction. Seeded growth occurs selectively on the $Cu_{1.8}S$ domain to form SnPdPtRhIr–$Cu_{1.8}S$–ZnS. (c) A line scan across one of the high entropy alloy regions (indicated by the yellow arrow that corresponds to the region highlighted in a yellow dashed box) confirms the presence and colocalization of all five metals. All scale bars are 20 nm.

Conclusion

In conclusion, we designed, synthesized, and characterized a 36-member library of nanoparticles comprising all pairwise seeded growth combinations of the metals Sn, Pd, Pt, Rh, Ir, and SnPdPtRhIr on the metal sulfides $Cu_{1.8}S$, ZnS, Co_9S_8, $CuInS_2$, $CuGaS_2$, and (Cu,Zn,Co,In,Ga)S.

This library included the (Cu,Zn,Co,In,Ga)S–SnPdPtRhIr hybrid nanoparticle construct that interfaces the high entropy metal sulfide (Cu,Zn,Co,In,Ga)S, which was identified as a semiconductor having a visible-wavelength band gap, with the high entropy alloy SnPdPtRhIr, which was identified as an active catalyst for the hydrogen evolution reaction under acidic conditions. By analyzing the growth behaviors, chemical compositions, and morphologies of the complete 36-member nanoparticle library, we were able to establish the primary factors that underpin successful seeded growth in this model 10-metal high entropy system. We found that the seeded growth of SnPdPtRhIr required temperatures near 275 ºC to facilitate incorporation of all five elements. We also found that growth of the high entropy alloy on the high entropy metal sulfide is enabled by cations in the metal sulfide that are capable of oxidizing, which concomitantly triggers reduction of the metal. By studying the seeded growth of the individual metals on the metal sulfides, we found that systems exhibiting minimal seeded growth behavior correlate with those that have the strongest metal-metal bond strengths, favoring growth on pre-existing metals rather than nucleation of new particles on the metal sulfide seeds. A careful interplay among relative metal-metal bond strengths appears to significantly influence the seeded growth behavior, including both composition and morphology. The scope of insights we gained allowed us to identify and disentangle the various competitive and synergistic chemical reactivities that are implicated in seeded growth in such compositionally complex systems. A resulting reactivity map provides practical guidelines for implementing seeded growth across a compositionally diverse range of nanoparticle systems, including high entropy alloys and their constituent metals on high entropy metal sulfides and their constituent metal sulfides. These insights are essential for designing and synthesizing next-generation multi-component nanostructures, across a wide range of applications, that incorporate the growing number of high entropy nanoparticles that are becoming synthetically accessible. This work therefore lays the groundwork for merging nanoparticle seeded growth with compositionally complex high entropy nanoparticles.

Experimental Section

Chemicals. Benzyl ether [99%] was purchased from ThermoScientific. Copper(II) chloride [$CuCl_2$, 97%], oleylamine [70%, technical grade], octadecene [90%, technical grade], di-*tert*-butyl disulfide [DTBDS, 97%], cobalt(II) chloride [$CoCl_2$, 97%], zinc(II) chloride [$ZnCl_2$, ≥97% ACS reagent grade, anhydrous], tin(II) chloride [$SnCl_2$, reagent grade, 98%], palladium(II) acetylacetonate [$Pd(acac)_2$, 99%], rhodium(III) acetylacetonate [$Rh(acac)_3$, 97%], and tetrachloroethylene [TCE, anhydrous ≥ 99%] were purchased from Millipore-Sigma. Indium(III) chloride [$InCl_3$, 98+%], platinum(II) acetylacetonate [$Pt(acac)_2$, ≥48.0% Pt], and iridium(IV) chloride [$IrCl_4$, ≥56.5% Ir] were purchased from Alfa Aesar. Gallium (III) chloride [$GaCl_3$, >98% anhydrous] and trioctylphosphine [TOP, >85%] were purchased from TCI America. Vulcan XC-72R was purchased from Fuel Cell Store. Commercial platinum 5 wt% on carbon (Pt/C) was purchased from Strem Chemicals. All solvents, including hexanes, isopropanol [IPA], toluene, and acetone, were of analytical grade. All the above chemicals were used as received without further purification. The metal chloride salts, except for $CuCl_2$, were stored in a glove box until they were used.

Synthesis of $Cu_{1.8}S$ nanoparticles. The synthesis of the $Cu_{1.8}S$ nanoparticle seeds was based on a previously reported procedure[53,54] where 341 mg of $CuCl_2$, 47 mL of oleylamine, and 11.8 mL of octadecene were first added to a 100 mL three neck round bottom flask equipped with a rubber septum, thermocouple, reflux condenser, gas flow adapter, and magnetic stir bar. This setup was connected to a Schlenk line and the flask was placed in a heating mantle. While stirring, the contents of the flask were placed under vacuum and heated to 100 ºC and held there for 30 minutes. At the same time, 8.25 mL of DTBDS was added to a 20 mL septum capped vial and placed under vacuum for at least 15 minutes. Both the vial and the flask were then cycled 3 times between vacuum and Ar after which the vial was removed from the Schlenk line, and the flask was placed under Ar flow. The flask was then heated to 200 °C and held at that temperature for 1 hour. At around 160 °C it could be observed that the flask changed from a dark blue to a yellow color, indicating the reduction of Cu^{2+} to Cu^{+}. The flask was then cooled to 180 °C and 8 mL of the DTBDS was rapidly injected. Once the flask recovered back to 180 °C, the reaction was allowed to proceed for 15 minutes. The flask was then quenched to room temperature using a water bath. Finally, the contents of the flask were poured into centrifuge tubes and mixed with a 1:1 mixture of IPA:acetone. The tubes were then placed into a centrifuge and were spun at a rate of 13,500 rpm for a total of 3 minutes. The supernatant was discarded and the pellet was resuspended in toluene. The resuspended nanospheres were then mixed with 1:1 IPA:acetone and the centrifugation process was repeated two more times for a total of three washes. Finally, the nanoparticles were suspended in hexanes to be used for subsequent reactions and further characterization.

***Preparation of metal cation exchange solutions*.** Metal salt solutions were first prepared by adding 100 mg of a metal chloride salt ($ZnCl_2$, $CoCl_2$, $InCl_3$, or $GaCl_3$), 15 mL of benzyl ether, 8 mL of oleylamine, and 2 mL of octadecene were placed in a 50 mL three neck round bottom flask equipped with a rubber septum, thermocouple, reflux condenser, gas flow adapter, and magnetic stir bar. (For $GaCl_3$, benzyl ether was replaced with an equivalent volume of additional octadecene to maximize stability of the precursor solution.) While stirring, the reaction setup was then connected to a Schlenk line, placed under vacuum, heated to 100 °C, and held at that temperature for 1 hour. Following that step, the flask was then cycled three times between Ar and vacuum, and finally left under an Ar blanket. The contents of the flask were then heated to 180 °C and held at that temperature for 30 minutes to allow the metal to complex with the oleylamine in solution. Finally, the flask was cooled to room temperature and the contents were poured into a 40 mL vial to be used for future cation exchange reactions.

Individual metal cation exchange reactions. All cation exchange reactions were based on an adaptation of a previously reported procedure[55,56] where we began by drying and weighing out in a 20 mL septum capped vial approx. 15 mg of $Cu_{1.8}S$ nanoparticles. The vial was then cycled three times between vacuum and Ar. Once under the inert Ar atmosphere, TOP was injected into the vial and the particles were sonicated for 45 minutes to ensure sufficient suspension. Next, 15 mL of benzyl ether, 8 mL of oleylamine, 2 mL of octadecene, and 2.5 times excess metal cation exchange solution (relative to a stoichiometric exchange, as shown in Table S2 of the Supporting Information) was added to fully replace all of the Cu^{+} cations in the $Cu_{1.8}S$ nanoparticles were added to a 50 mL three neck round bottom flask equipped with a rubber septum, thermocouple, reflux condenser, gas flow adapter, and magnetic stir bar. The flask was then connected to a Schlenk line, set to stir, placed under vacuum, heated to 100 °C, and held at that temperature for 1 hour. The flask was then cycled three times between vacuum and Ar where it was finally placed under an Ar blanket and heated to 180 °C. After 30 minutes at 180 °C, the flask was cooled to the required reaction temperature (100 °C for Co^{2+}, 120 °C for Zn^{2+}, 110 °C for In^{3+}, and 140 °C for Ga^{3+}). Once settled at the specified temperature, the TOP/$Cu_{1.8}S$ mixture was rapidly injected and the reaction was allowed to proceed for 30 minutes. The reaction was then quenched via an ice bath and allowed to cool until the temperature was below 15 °C, which prevented etching of any remaining $Cu_{1.8}S$ nanoparticles. The contents of the flask were then poured into centrifuge tubes, mixed with a 1:1 mixture of IPA:acetone, and centrifuged at 13,500 rpm for 3 minutes. The supernatant was discarded and the remaining pellet was resuspended in toluene. A 1:1 mixture of IPA:acetone was again added to the tubes and the centrifugation process was repeated for a second time. The particles were then resuspended in hexanes for use in future reactions.

(Cu,Zn,Co,In,Ga)S high entropy metal sulfide cation exchange reaction. The reaction to synthesize the high entropy metal sulfide was carried out in much the same manner as the single metal cation exchange reactions described above and was modified from a previous report.[25] Here, all four metal cation exchange solutions were combined in the same flask and the excess amounts were modified. Assuming exactly 15 mg of $Cu_{1.8}S$ spheres, the stoichiometric cation amounts (and the volumes of the metal cation exchange solutions) were 0.2 times excess Co^{2+} (0.34 mL), 0.3 times excess In^{3+} (0.57 mL), 0.3 times excess Zn^{2+} (0.53 mL), and 0.4 times excess Ga^{3+} (0.61 mL). These amounts provided a small 1.2 times excess to ensure complete exchange of the Cu^+ cations, coupled with the knowledge that Co^{2+} exchanges very rapidly so a smaller excess was sufficient and Ga^{3+} exchanges relatively slowly so a larger excess was necessary. This reaction was carried out at 140 ^{o}C, which corresponded to the highest temperature required to exchange any of the constituent metal cations (*i.e.*, Ga^{3+}).

Metal seeded growth solutions. Metal salt solutions for synthesizing and growing the high entropy alloy and its constituent metals were prepared by dissolving 0.1054 mmol of each metal salt [42.2 mg $Rh(acac)_3$, 32.2 mg $Pd(acac)_2$, 35.2 mg $IrCl_4$, 41.4 mg $Pt(acac)_2$, 19.8 mg $SnCl_2$] in 10 mL of oleylamine with a stir bar in a 20 mL vial. The vial was then heated to 120 ^{o}C and held at that temperature until the metal salt was fully dissolved. The metal salts were chosen to remain consistent with a prior report.[20]

Seeded growth reactions. The seeded growth of the high entropy alloy and individual metals was carried out using a modification of a published procedure used to synthesize the high entropy alloy directly.[20] Briefly, approx. 5 mg of dried metal sulfide nanoparticles were placed in a 20 mL septum capped vial. The nanoparticles were then suspended in 6 mL of oleylamine and transferred to a 50 mL three neck round bottom flask equipped with a rubber septum, thermocouple, reflux condenser, gas flow adapter, and magnetic stir bar. Next, 10 mL of octadecene was then added to the flask, which was placed under vacuum, heated to 110 ^{o}C while stirring, and held at that temperature for 30 minutes. In the meantime, the appropriate metal deposition solutions were heated to 120 ^{o}C while being stirred, and then 1 mL of total metal deposition solution (0.2 mL of each metal deposition for the high entropy alloy) was added to a 20 mL septum capped vial along with 4 mL of oleylamine and a stir bar. The vial was then placed under vacuum while stirring and allowed to sit for 15 minutes. At this point, the flask with the metal sulfide nanoparticles was cycled three times between Ar and vacuum and left under an Ar blanket. The flask was then heated to 275 ^{o}C and the septum capped vial was cycled three times between Ar and vacuum. Once the flask reached 275 ^{o}C, 4 mL of the metal deposition solution in the septum capped vial was slowly injected into the flask at a rate of 0.4 mL/min (10 minute total injection time). After the injection finished, the flask was first cooled in air to 200 ^{o}C, followed by quenching using a water bath. The particles were then poured into a centrifuge tube, mixed with 1:1 IPA:acetone, and centrifuged at 14,500 rpm for 3 minutes. The supernatant was then discarded and the pellet was resuspended in toluene. Again, a 1:1 mixture of IPA:acetone was added back into the centrifuge tubes and the centrifugation process was repeated once more. Finally, the particles were resuspended in hexanes.

Electrochemical Measurements. All electrochemical measurements were conducted using a Gamry Instruments Reference 1000B Potentiostat. Electrochemical measurements were performed in a 200 mL 4-neck round bottom flask with a Compact Pine Rotator rotating disk electrode (RDE) setup, using 150 mL 0.5 M H_2SO_4 (99.999%) as the electrolyte, a graphite rod as the counter electrode, and a saturated calomel electrode (SCE) as the reference electrode. To prepare the carbon loaded sample, 5 mg of nanoparticles and 20 mg commercial carbon black (Vulcan XC-72R) were dispersed in 10 mL of cyclohexanes and sonicated for 3 h to achieve a loading of ~20 wt%. The product was washed three times with acetone, collected by centrifugation, and left to dry under vacuum. Next, to remove surface ligands, the obtained black powder was heated to 450 °C under 5% H_2/Ar flow for 1 h. The working electrode was prepared by dispersing 5 mg of the prepared catalyst in 800 µL of water, 180 µL of isopropanol, and 20 µL of 5 wt% Nafion solution, and then sonicating for 1 h. Subsequently, 10.0 µL of the catalyst ink was dropped onto a glassy carbon electrode (5 mm diameter, sonicated in acetone, ethanol, and water for cleaning and polished with diamond paste prior to use), and dried. All electrochemical measurements were carried out in a 0.5 M H_2SO_4 electrolyte. The 0.5 M H_2SO_4 electrolyte was bubbled with Ar for 30 min prior to any testing. Also prior to testing, the working electrodes were cleaned by a CV scan at 0.05-0.4 V (vs RHE) for 100 cycles at a rate of 250 mV/s until a stable CV curve was obtained. All linear sweep voltammetry scans were run at a rotation speed of 1600 RPM. Linear sweep voltammetry (LSV) scans were run at a scan rate of 25 mV/s and utilized the current interrupt (CI) method to correct for iR-drop caused by uncompensated resistance.

Characterization. Powder X-Ray diffraction (XRD) data were collected using a Malvern PANalytical Empyrean with either Cu Kα radiation or Co Kα radiation as the X-ray source. Cu Kα radiation was used for most samples. For the samples containing Co_9S_8, Co Kα radiation was used instead to suppress Co fluorescence. Transmission electron microscopy (TEM) images, high-angle annular dark field scanning transmission electron microscopy (HAADF-STEM) images, and STEM energy dispersive X-ray spectroscopy (STEM-EDS) maps were collected using an FEI Talos F200X S/TEM operating at 200 kV. The EDS maps for each element consisted of the Cu K lines, Zn K lines, Co K lines, Ga K lines, In L lines, Pd L lines, Rh L lines, Sn L lines, Pt L lines, Ir L lines, and S K lines. Velox 3.6.0 software was used to analyze the STEM-EDS element map data. All simulated diffraction patterns were generated using CrystalDiffract which is distributed by CrystalMaker Software Ltd., Oxford, England (www.crystalmaker.com). Simulated XRD patterns, for reference, were obtained from literature references. Ultraviolet-visible-near infrared (UV-vis-NIR) absorption data were collected on a PerkinElmer LAMBDA 950 UV-vis NIR spectrometer using a standard detector and quartz spectrophotometer cell from Stama Cells, Inc., with a data interval of 2 nm. All UV-vis samples were suspended in tetrachloroethylene and briefly sonicated before data collection.

ASSOCIATED CONTENT

Supporting Information

The Supporting Information is available free of charge on the ACS Publications website.

- Additional experimental information and supplementary TEM, STEM-EDS, and XRD data (PDF).

AUTHOR INFORMATION

Corresponding Author

Raymond E. Schaak – *Department of Chemistry*, *Department of Chemical Engineering*, and *Materials Research Institute*, *The Pennsylvania State University, University Park, Pennsylvania 16802, United States*; Email: res20@psu.edu

Authors

Joseph M. Veglak – *Department of Chemistry*, *The Pennsylvania State University, University Park, Pennsylvania 16802, United States*

Aaron Tsai – *Department of Chemistry*, *The Pennsylvania State University, University Park, Pennsylvania 16802, United States*

Samuel S. Soliman – *Department of Chemistry*, *The Pennsylvania State University, University Park, Pennsylvania 16802, United States*

Gaurav R. Dey – *Department of Chemistry*, *The Pennsylvania State University, University Park, Pennsylvania 16802, United States*

Notes

The authors declare no competing financial interest.

ACKNOWLEDGMENT

This work was supported by the U.S. National Science Foundation under grant CHE-2203353. TEM, XRD, and UV-Vis data were acquired at the Materials Characterization Lab of the Penn State Materials Research Institute. J.M.V. also acknowledges Jennifer Gray and Ke Wang for assistance with electron microscopy, Kate Baumler for assistance with XRD using a Co source, Sarah O'Boyle for assistance with graphic design, and Alex Leffel for helpful discussions.

REFERENCES

(1) Ren, J.-T.; Chen, L.; Wang, H.-Y.; Yuan, Z.-Y. High-Entropy Alloys in Electrocatalysis: From Fundamentals to Applications. *Chem. Soc. Rev.* **2023**, *52*, 8319-8373. https://doi.org/10.1039/D3CS00557G.

(2) Wen, Y.; Zhang, W.; Wang, X.; Lu, S.; Duan, F.; Zhu, H.; Du, M. Dual Phase B-Doped FeCoNiCuPd High-Entropy Alloys for Nitrogen Electroreduction to Ammonia. *Chem. Commun.* **2023**, *59*, 13371-13374. https://doi.org/10.1039/D3CC04581A.

(3) Xin, Y.; Li, S.; Qian, Y.; Zhu, W.; Yuan, H.; Jiang, P.; Guo, R.; Wang, L. High-Entropy Alloys as a Platform for Catalysis: Progress, Challenges, and Opportunities. *ACS Catal.* **2020**, *10* (19), 11280–11306. https://doi.org/10.1021/acscatal.0c03617.

(4) Sun, Y.; Dai, S. High-Entropy Materials for Catalysis: A New Frontier. *Science Advances* **2021**, *7* (20), eabg1600. https://doi.org/10.1126/sciadv.abg1600.

(5) Kumari, P.; Gupta, A. K.; Mishra, R. K.; Ahmad, M. S.; Shahi, R. R. A Comprehensive Review: Recent Progress on Magnetic High Entropy Alloys and Oxides. *Journal of Magnetism and Magnetic Materials* **2022**, *554*, 169142. https://doi.org/10.1016/j.jmmm.2022.169142.

(6) Chaudhary, V.; Chaudhary, R.; Banerjee, R.; Ramanujan, R. V. Accelerated and Conventional Development of Magnetic High Entropy Alloys. *Materials Today* **2021**, *49*, 231–252. https://doi.org/10.1016/j.mattod.2021.03.018.

(7) Chu, S.; Shao, C.; Tian, J.; Wang, J.; Rao, Y.; Xu, C.; Zhou, H.; Guo, S. High Entropy-Induced Kinetics Improvement and Phase Transition Suppression in K-Ion Battery Layered Cathodes. *ACS Nano* **2024**, *18* (1) 337-346. https://doi.org/10.1021/acsnano.3c06393.

(8) Zhao, Q.; Cao, Z.; Wang, X.; Chen, H.; Shi, Y.; Cheng, Z.; Guo, Y.; Li, B.; Gong, Y.; Du, Z.; Yang, S. High-Entropy Laminates with High Ion Conductivities for High-Power All-Solid-State Lithium Metal Batteries. *J. Am. Chem. Soc.* **2023**, *145* (38) 21242-21252. https://doi.org/10.1021/jacs.3c04279.

(9) Zeng, Y.; Ouyang, B.; Liu, J.; Byeon, Y.-W.; Cai, Z.; Miara, L. J.; Wang, Y.; Ceder, G. High-Entropy Mechanism to Boost Ionic Conductivity. *Science* **2022**, *378* (6626), 1320–1324. https://doi.org/10.1126/science.abq1346.

(10) Wang, X.; Yao, H.; Zhang, Z.; Li, X.; Chen, C.; Yin, L.; Hu, K.; Yan, Y.; Li, Z.; Yu, B.; Cao, F.; Liu, X.; Lin, X.; Zhang, Q. Enhanced Thermoelectric Performance in High Entropy Alloys $Sn_{0.25}Pb_{0.25}Mn_{0.25}Ge_{0.25}Te$. *ACS Appl. Mater. Interfaces* **2021**, *13* (16), 18638–18647. https://doi.org/10.1021/acsami.1c00221.

(11) Luo, Y.; Hao, S.; Cai, S.; Slade, T. J.; Luo, Z. Z.; Dravid, V. P.; Wolverton, C.; Yan, Q.; Kanatzidis, M. G. High Thermoelectric Performance in the New Cubic Semiconductor $AgSnSbSe_3$ by High-Entropy Engineering. *J. Am. Chem. Soc.* **2020**, *142* (35), 15187–15198. https://doi.org/10.1021/jacs.0c07803.

(12) Yao, Y.; Huang, Z.; Xie, P.; Lacey, S. D.; Jacob, R. J.; Xie, H.; Chen, F.; Nie, A.; Pu, T.; Rehwoldt, M.; Yu, D.; Zachariah, M. R.; Wang, C.; Shahbazian-Yassar, R.; Li, J.; Hu, L. Carbothermal Shock Synthesis of High-Entropy-Alloy Nanoparticles. *Science* **2018**, *359* (6383), 1489–1494. https://doi.org/10.1126/science.aan5412.

(13) Qiao, H.; Saray, M. T.; Wang, X.; Xu, S.; Chen, G.; Huang, Z.; Chen, C.; Zhong, G.; Dong, Q.; Hong, M.; Xie, H.; Shahbazian-Yassar, R.; Hu, L. Scalable Synthesis of High Entropy Alloy Nanoparticles by Microwave Heating. *ACS Nano* **2021**, *15* (9), 14928–14937. https://doi.org/10.1021/acsnano.1c05113.

(14) Yao, Y.; Huang, Z.; Hughes, L. A.; Gao, J.; Li, T.; Morris, D.; Zeltmann, S. E.; Savitzky, B. H.; Ophus, C.; Finfrock, Y. Z.; Dong, Q.; Jiao, M.; Mao, Y.; Chi, M.; Zhang, P.; Li, J.; Minor, A. M.; Shahbazian-Yassar, R.; Hu, L. Extreme Mixing in Nanoscale Transition Metal Alloys. *Matter* **2021**, *4* (7), 2340–2353. https://doi.org/10.1016/j.matt.2021.04.014.

(15) Yang, Y.; Song, B.; Ke, X.; Xu, F.; Bozhilov, K. N.; Hu, L.; Shahbazian-Yassar, R.; Zachariah, M. R. Aerosol Synthesis of High Entropy Alloy Nanoparticles. *Langmuir* **2020**, *36* (8), 1985–1992. https://doi.org/10.1021/acs.langmuir.9b03392.

(16) Dey, G. R.; Soliman, S. S.; McCormick, C. R.; Wood, C. H.; Katzbaer, R. R.; Schaak, R. E. Colloidal Nanoparticles of High Entropy Materials: Capabilities, Challenges, and Opportunities in Synthesis and Characterization. *ACS Nanosci. Au* **2024**, *4*, (1) 3-20. https://doi.org/10.1021/acsnanoscienceau.3c00049.

(17) Soliman, S. S.; Dey, G. R.; McCormick, C. R.; Schaak, R. E. Temporal Evolution of Morphology, Composition, and Structure in the Formation of Colloidal High-Entropy Intermetallic Nanoparticles. *ACS Nano* **2023**, *17* (16), 16147–16159. https://doi.org/10.1021/acsnano.3c05241.

(18) Li, H.; Han, Y.; Zhao, H.; Qi, W.; Zhang, D.; Yu, Y.; Cai, W.; Li, S.; Lai, J.; Huang, B.; Wang, L. Fast Site-to-Site Electron Transfer of High-Entropy Alloy Nanocatalyst Driving Redox Electrocatalysis. *Nat Commun* **2020**, *11* (1), 5437. https://doi.org/10.1038/s41467-020-19277-9.

(19) Broge, N. L. N.; Bondesgaard, M.; Søndergaard-Pedersen, F.; Roelsgaard, M.; Iversen, B. B. Autocatalytic Formation of High-Entropy Alloy Nanoparticles. *Angewandte Chemie* **2020**, *132* (49), 22104–22108. https://doi.org/10.1002/ange.202009002.

(20) Dey, G. R.; McCormick, C. R.; Soliman, S. S.; Darling, A. J.; Schaak, R. E. Chemical Insights into the Formation of Colloidal High Entropy Alloy Nanoparticles. *ACS Nano* **2023**, *17* (6), 5943–5955. https://doi.org/10.1021/acsnano.3c00176.

(21) Wu, D.; Kusada, K.; Yamamoto, T.; Toriyama, T.; Matsumura, S.; Kawaguchi, S.; Kubota, Y.; Kitagawa, H. Platinum-Group-Metal High-Entropy-Alloy Nanoparticles. *J. Am. Chem. Soc.* **2020**, *142* (32), 13833–13838. https://doi.org/10.1021/jacs.0c04807.

(22) Chen, Y.; Zhan, X.; Bueno, S. L. A.; Shafei, I. H.; Ashberry, H. M.; Chatterjee, K.; Xu, L.; Tang, Y.; Skrabalak, S. E. Synthesis of Monodisperse High Entropy Alloy Nanocatalysts from Core@shell Nanoparticles. *Nanoscale Horiz.* **2021**, *6* (3), 231–237. https://doi.org/10.1039/D0NH00656D.

(23) Bueno, S. L. A.; Leonardi, A.; Kar, N.; Chatterjee, K.; Zhan, X.; Chen, C.; Wang, Z.; Engel, M.; Fung, V.; Skrabalak, S. E. Quinary, Senary, and Septenary High Entropy Alloy Nanoparticle Catalysts from Core@Shell Nanoparticles and the Significance of Intraparticle Heterogeneity. *ACS Nano* **2022**, *16* (11), 18873–18885. https://doi.org/10.1021/acsnano.2c07787.

(24) Kar, N.; McCoy, M.; Wolfe, J.; Bueno, S. L. A.; Shafei, I. H.; Skrabalak, S. E. Retrosynthetic Design of Core–Shell Nanoparticles for Thermal Conversion to Monodisperse High-Entropy Alloy Nanoparticles. *Nat. Synth* **2024**, *3* (2), 175–184. https://doi.org/10.1038/s44160-023-00409-0.

(25) McCormick, C. R.; Schaak, R. E. Simultaneous Multication Exchange Pathway to High-Entropy Metal Sulfide Nanoparticles. *J. Am. Chem. Soc.* **2021**, *143* (2), 1017–1023. https://doi.org/10.1021/jacs.0c11384.

(26) Theibault, M. J.; McCormick, C. R.; Lang, S.; Schaak, R. E.; Abruña, H. D. High Entropy Sulfide Nanoparticles as Lithium Polysulfide Redox Catalysts. *ACS Nano* **2023**, *17* (18), 18402–18410. https://doi.org/10.1021/acsnano.3c05869.

(27) Mumme, W. G.; Gable, R. W.; Petříček, V. THE CRYSTAL STRUCTURE OF ROXBYITE, $Cu_{58}S_{32}$. *The Canadian Mineralogist* **2012**, *50* (2), 423–430. https://doi.org/10.3749/canmin.50.2.423.

(28) Williamson, E. M.; Sun, Z.; Mora-Tamez, L.; Brutchey, R. L. Design of Experiments for Nanocrystal Syntheses: A How-To Guide for Proper Implementation. *Chem. Mater.* **2022**, *34* (22), 9823–9835. https://doi.org/10.1021/acs.chemmater.2c02924.

(29) Mints, V. A.; Pedersen, J. K.; Bagger, A.; Quinson, J.; Anker, A. S.; Jensen, K. M. Ø.; Rossmeisl, J.; Arenz, M. Exploring the Composition Space of High-Entropy Alloy Nanoparticles for the Electrocatalytic H_2/CO Oxidation with Bayesian Optimization. *ACS Catal.* **2022**, *12* (18), 11263–11271. https://doi.org/10.1021/acscatal.2c02563.

(30) Xu, Y.-N.; Ching, W. Y. Electronic, Optical, and Structural Properties of Some Wurtzite Crystals. *Phys. Rev. B* **1993**, *48* (7), 4335–4351. https://doi.org/10.1103/PhysRevB.48.4335.

(31) Rajamani, V.; Prewitt, C. T. Refinement of the Structure of Co9S8. *Can. Mineral.* **1975**, *13*, 75–78.

(32) Huang, W.-C.; Tseng, C.-H.; Chang, S.-H.; Tuan, H.-Y.; Chiang, C.-C.; Lyu, L.-M.; Huang, M. H. Solvothermal Synthesis of Zincblende and Wurtzite $CuInS_2$ Nanocrystals and Their Photovoltaic Application. *Langmuir* **2012**, *28* (22), 8496–8501. https://doi.org/10.1021/la300742p.

(33) Xiao, N.; Zhu, L.; Wang, K.; Dai, Q.; Wang, Y.; Li, S.; Sui, Y.; Ma, Y.; Liu, J.; Liu, B.; Zou, G.; Zou, B. Synthesis and High-Pressure Transformation of Metastable Wurtzite-Structured $CuGaS_2$ Nanocrystals. *Nanoscale* **2012**, *4* (23), 7443–7447. https://doi.org/10.1039/C2NR31629C.

(34) Wark, S. E.; Hsia, C.-H.; Son, D. H. Effects of Ion Solvation and Volume Change of Reaction on the Equilibrium and Morphology in Cation-Exchange Reaction of Nanocrystals. *J. Am. Chem. Soc.* **2008**, *130* (29), 9550–9555. https://doi.org/10.1021/ja802187c.

(35) Park, J.; Jin, H.; Lee, J.; Oh, A.; Kim, B.; Kim, J. H.; Baik, H.; Joo, S. H.; Lee, K. Highly Crystalline $Pd_{13}Cu_3S_7$ Nanoplates Prepared via Partial Cation Exchange of $Cu_{1.81}S$ Templates as an Efficient Electrocatalyst for the Hydrogen Evolution Reaction. *Chem. Mater.* **2018**, *30* (19), 6884–6892. https://doi.org/10.1021/acs.chemmater.8b03178.

(36) Leonard, B. M.; Schaak, R. E. Multistep Solution-Mediated Formation of $AuCuSn_2$: Mechanistic Insights for the Guided Design of Intermetallic Solid-State Materials and

Complex Multimetal Nanocrystals. *J. Am. Chem. Soc.* **2006**, *128* (35), 11475–11482. https://doi.org/10.1021/ja062475h.

(37) Cable, R. E.; Schaak, R. E. Low-Temperature Solution Synthesis of Nanocrystalline Binary Intermetallic Compounds Using the Polyol Process. *Chem. Mater.* **2005**, *17* (26), 6835–6841. https://doi.org/10.1021/cm0520113.

(38) Wang, X.; Stöver, J.; Zielasek, V.; Altmann, L.; Thiel, K.; Al-Shamery, K.; Bäumer, M.; Borchert, H.; Parisi, J.; Kolny-Olesiak, J. Colloidal Synthesis and Structural Control of PtSn Bimetallic Nanoparticles. *Langmuir* **2011**, *27* (17), 11052–11061. https://doi.org/10.1021/la201829y.

(39) Kovnir, K.; Schmidt, M.; Waurisch, C.; Armbrüster, M.; Prots, Y.; Grin, Y. Refinement of the crystal structure of dipalladium gallium, Pd_2Ga. *Zeitschrift für Kristallographie - New Crystal Structures* **2008**, *223* (1), 7–8. https://doi.org/10.1524/ncrs.2008.0004.

(40) Gronvold, F.; Rost, E. The Crystal Structures of Pd_4Se and Pd_4S. *Acta Crystallographica* **1962**, *15*, 11–13.

(41) Harris, I. R.; Norman, M.; Gardner, W. E. The Electronic State of Cerium in Some $CeRh_{3-x}Pd_x$ Alloys. *Journal of the Less Common Metals* **1972**, *29* (3), 299–309. https://doi.org/10.1016/0022-5088(72)90118-X.

(42) Brooksbank, D.; Andrews, K.W. Thermal Expansion of Some Inclusions Found in Steels and Relation to Tessellated Stresses. *Journal of the Iron and Steel Institute* **1968**, *206*, 595-599

(43) Ross, R. G.; Hume-Rothery, W. High Temperature X-Ray Metallography: I. A New Debye-Scherrer Camera for Use at Very High Temperatures II. A New Parafocusing Camera III. Applications to the Study of Chromium, Hafnium, Molybdenum, Rhodium, Ruthenium and Tungsten. *Journal of the Less Common Metals* **1963**, *5* (3), 258–270. https://doi.org/10.1016/0022-5088(63)90031-6.

(44) Schröder, R. H.; Schmitz-Pranghe, N.; Kohlhaas, R. Experimentelle Bestimmung der Gitterparameter der Platinmetalle imTemperaturbereich von 190 bis 1709 °C. *Zeitschrift fuer Metallkunde* **1972**, *63*, 12-16.

(45) Sun, Y.; Wang, Y.; Chen, J. Y. C.; Fujisawa, K.; Holder, C. F.; Miller, J. T.; Crespi, V. H.; Terrones, M.; Schaak, R. E. Interface-Mediated Noble Metal Deposition on Transition Metal Dichalcogenide Nanostructures. *Nat. Chem.* **2020**, *12* (3), 284–293. https://doi.org/10.1038/s41557-020-0418-3.

(46) Haynes, W. M. *CRC Handbook of Chemistry and Physics*, 95th ed.; CRC Press, Taylor & Francis: Boca Raton, FL 2014.

(47) Wang, X.; Qin, Z.; Qian, J.; Chen, L.; Shen, K. IrCo Nanoparticles Encapsulated with Carbon Nanotubes for Efficient and Stable Acidic Water Splitting. *ACS Catal.* **2023**, *13* (16), 10672–10682. https://doi.org/10.1021/acscatal.3c02887.

(48) Cao, D.; Wang, J.; Zhang, H.; Xu, H.; Cheng, D. Growth of IrCu Nanoislands with Rich IrCu/Ir Interfaces Enables Highly Efficient Overall Water Splitting in Non-Acidic Electrolytes. *Chemical Engineering Journal* **2021**, *416*, 129128. https://doi.org/10.1016/j.cej.2021.129128.

(49) Kwon, T.; Hwang, H.; Sa, Y. J.; Park, J.; Baik, H.; Joo, S. H.; Lee, K. Cobalt Assisted Synthesis of IrCu Hollow Octahedral Nanocages as Highly Active Electrocatalysts toward Oxygen Evolution Reaction. *Advanced Functional Materials* **2017**, *27* (7), 1604688. https://doi.org/10.1002/adfm.201604688.

(50) Huang, X.; Su, Y.; Sai, L.; Zhao, J.; Kumar, V. Low-Energy Structures of Binary Pt–Sn Clusters from Global Search Using Genetic Algorithm and Density Functional Theory. *J Clust Sci* **2015**, *26* (2), 389–409. https://doi.org/10.1007/s10876-014-0829-7.

(51) Veglak, J. M.; Jeong, C.-H.; Young, H. L.; O'Boyle, S. K.; Schaak, R. E. Using Cation-Exchanged Nanorod Templates To Direct the Regioselective Growth and Plasmonic Coupling of Gold Nanoparticles. *ACS Materials Lett.* **2023**, *5* (11), 3000–3006. https://doi.org/10.1021/acsmaterialslett.3c01116.

(52) Fenton, J. L.; Steimle, B. C.; Schaak, R. E. Tunable Intraparticle Frameworks for Creating Complex Heterostructured Nanoparticle Libraries. *Science* **2018**, *360* (6388), 513–517. https://doi.org/10.1126/science.aar5597.

(53) O'Boyle, S. K.; Fagan, A. M.; Steimle, B. C.; Schaak, R. E. Expanded Tunability of Intraparticle Frameworks in Spherical Heterostructured Nanoparticles through Substoichiometric Partial Cation Exchange. *ACS Mater. Au* **2022**, *2* (6), 690–698. https://doi.org/10.1021/acsmaterialsau.2c00038.

(54) McCormick, C. R.; Baksa, S. M.; Veglak, J. M.; Dabo, I.; Schaak, R. E. Chemical Insights into the Formation of Metastable Zinc Cobalt Sulfide Solid-Solution Nanoparticles through Simultaneous Multi-Cation Exchange. *Chem. Mater.* **2023**, *35* (14), 5433–5446. https://doi.org/10.1021/acs.chemmater.3c00763.

(55) Steimle, B. C.; Fagan, A. M.; Butterfield, A. G.; Lord, R. W.; McCormick, C. R.; Di Domizio, G. A.; Schaak, R. E. Experimental Insights into Partial Cation Exchange Reactions for Synthesizing Heterostructured Metal Sulfide Nanocrystals. *Chem. Mater.* **2020**, *32* (13), 5461–5482. https://doi.org/10.1021/acs.chemmater.0c01388.

(56) Butterfield, A. G.; McCormick, C. R.; Veglak, J. M.; Schaak, R. E. Morphology-Dependent Phase Selectivity of Cobalt Sulfide during Nanoparticle Cation Exchange Reactions. *J. Am. Chem. Soc.* **2021**, *143* (21), 7915–7919. https://doi.org/10.1021/jacs.1c03478.

Table of Contents Graphic